Amorphization of Pseudocapacitive T—Nb$_2$O$_5$ Accelerates Lithium Diffusivity as Revealed Using Tunable Isomorphic Architectures

Wessel van den Bergh,[a] Sean Wechsler,[a] Hasala Nadeesini Lokupitiya,[a] Lauren Jarocha,[b] Kwangnam Kim,[c] James Chapman,[c] Kyoung E. Kweon,[c] Brandon C. Wood,[c] Steve Heald,[d] and Morgan Stefik*[a]

Intercalation pseudocapacitance can combine capacitor-like power densities with battery-like energy densities. Such surface-limited behavior requires rapid diffusion where amorphization can increase solid-state diffusivity. Here intercalation pseudocapacitive materials with tailored extents of amorphization in T-Nb$_2$O$_5$ are first reported. Amorphization was characterized with WAXS, XPS, XAFS, and EPR which suggested a peroxide-rich (O$_2^{2-}$) surface that was consistent with DFT predictions. A series of tunable isomorphic architectures enabled comparisons while independently varying transport parameters. Through process of elimination, solid-state lithium diffusion was identified as the dominant diffusive-constraint dictating the maximum voltage sweep rate for surface-limited kinetics (v_{SLT}), termed the Surface-Limited Threshold (SLT). The v_{SLT} increased with amorphization however stable cycling required crystalline T-Nb$_2$O$_5$. A current-response model using series-impedances well-matched these observations. This perspective revealed that amorphization of T-Nb$_2$O$_5$ enhanced solid-state diffusion by 12.2% and increased surface-limitations by 17.0% (stable samples). This approach enabled retaining 95% lithiation capacity at ~800 mV s^{-1} (1,600 C-rate equivalent).

Introduction

The broad demand for electrochemical energy storage materials with high energy density and rapid (dis)charge times has motivated widespread research into new electrode chemistries and tailored electrode architectures.[1–6] Current lithium-ion batteries and electrochemical double-layer capacitors do not meet these simultaneous demands with the former suffering from sluggish solid-state kinetics and the latter from low energy density.[7–9] Pseudocapacitive[10–15] behavior combines rapid surface-limited kinetics with faradaic energy storage mechanisms and is a path towards concomitant high power and energy densities. Early studies[16–18] on RuO$_2$ were the first reports of pseudocapacitance based upon faradaic surface reactions[16] but more recent work on orthorhombic ("Tief") T-Nb$_2$O$_5$ have identified a similar kinetic response with an intercalation-based mechanism.[19,20] Here the rate of lithiation naturally depends upon the nanoscale architecture and the implied transport pathlengths for electrons, electrolytes, and solid-state ion intercalation.[21] This concomitant set of transport processes along with the surface reaction determine the overall rate capability which may be limited by either diffusion processes or the surface reaction. With increasing voltage sweep rate (v), the transition from the surface-limited regime towards the diffusion-limited regime reflects the balance of these processes and was recently termed the surface-limited threshold (SLT).[21] Surface-limited kinetics are possible when the overall rate is not limited by diffusive processes and there is an absence of a crystallographic phase changes upon intercalation.[22–26] Numerous nanoscale niobia structures have been reported with an emphasis on individual performance metrics.[27–74] A few investigations have approached the relationship between nanostructure and T-Nb$_2$O$_5$ performance using computational models,[75] advanced electrochemical techniques,[76] tunable nanotubes,[77] and core-shell particles[78,79] without experimentally isolating the rate-limiting process(es). In contrast, changing a single transport parameter at a time recently enabled the first unambiguous identification of solid-state lithium diffusion as the dominant diffusion-limited process in T-Nb$_2$O$_5$ lithiation as a function of the extrinsic nanostructure.[21]

[a] W. van den Bergh, S. Wechsler, H. N. Lokupitiya, Prof. M. Stefik
Department of Chemistry and Biochemistry
University of South Carolina
Columbia, South Carolina 29208, United States
E-mail: stefik@mailbox.sc.edu

[b] L. Jarocha
Department of Chemistry
Furman University
Greenville, South Carolina 29613, United States

[c] K. Kim, J. Chapman, K. E. Kweon, B. C. Wood
Physical and Life Sciences Directorate
Lawrence Livermore National Laboratory
Livermore, California 94550, United States

[d] S. Heald
X-Ray Science Division
Advanced Photon Source, Argonne National Lab
Lemont, IL 60439, United States

Batteries & Supercaps

Research Article
doi.org/10.1002/batt.202200056

**Chemistry
Europe**

European Chemical
Societies Publishing

Solid-state lithium diffusivities vary widely with composition and crystal structure where amorphization is recently being explored as a route to accelerate known materials. Amorphization is broadly defined here as the deliberate inclusion of defects where the extent of amorphization spans the continuous gamut from perfect crystals to amorphous materials.[80] While the specific electrochemical observations vary widely, amorphization has sometimes led to increased performance[45,64,68,81–84] with diverse intercalation materials. Many past works have examined oxygen vacancies and dopants. Dopants are usually introduced to improve electrical conductivity with electron donating species[45,68] while oxygen vacancies have also improved electrical conductivity[81–83,85] in addition to enhanced lithium diffusivity,[64,82] increased lithiation capacity,[64,68,81–83] and enhanced stability[82] depending on the vacancy concentration. A recent comparison of crystalline anatase and amorphous TiO_2 reported the latter's higher diffusivity due to lower activation energy for Li hops between sites.[84,86] For T-Nb_2O_5 lithiation, some reports indicated amorphization of T-Nb_2O_5 via oxygen vacancies enhanced performance[64,68,83] whereas the amorphous phase itself had greatly lowered lithiation capacity and/or slower kinetics.[19,22,24,25,62,71] Past works have also compared lithiation performance of different Nb_2O_5 crystallographic phases.[22,24,25,57,62,71,87,88] Thermal treatments are conventionally used for crystallization (lowered amorphization). It should be recognized however that there is a continuum for the extent of amorphization along the path from an amorphous solid to a perfect crystal. One of the challenges when comparing samples from different heat treatments is that the nanoscale architecture may simultaneously change, convolving multiple variables and adding causal ambiguity. Here changes in specific electrochemical processes are attributed to tailored extent of T-Nb_2O_5 amorphization by comparing series of isomorphic nanoscale architectures to enable unambiguous interpretation.

The use of persistent micelle templates (PMT) enables the production of tunable isomorphic architectures that alter a single spatial-variable at a time.[21,89–93] With PMT, the material wall thickness is independently tailored while preserving a constant average pore diameter by using kinetically trapped micelles as templates. PMTs are based upon kinetic control where the solution conditions impose a large enthalpic barrier to polymer chain exchange between micelles.[21,89–93] Furthermore, the preservation of spherical micelle templates leads to isomorphic series with relatively constant tortuosity owing to simple sphere packing.[94] In contrast, typical block polymer-based methods rely upon equilibration which couples all architectural attributes as well as the morphology to free-energy minimization.[95,96] With PMT, the subsequent thermal treatment removes the micelle template and converts the material precursors to the desired material. The time and the temperature of this heat treatment reduces the extent of amorphization as the material further crystalizes. Here the effect of tailored amorphization upon the pseudocapacitive response of orthorhombic niobia nanostructures is systematically elaborated. Furthermore, a revised $i(v)$ model for CV is shown to be congruent with observations and enables

quantitative parsing of surface-limited and diffusion-limited contributions.

Results and Discussion

Both material and architecture determine electrode performance. Amorphization is known to augment material performance however the assessment of that change independently is challenging since modifications to heat treatments can simultaneously alter architectural parameters, for example, the pore size and wall thickness. On the other hand, the use of tunable isomorphic architectures provides a unique perspective to reveal architectural effects alone. Thus, a strategy combining material modifications (amorphization) in concert with controlled architectural variations can yield more direct insights to nanoscale cause-and-effect relationships. Here tunable isomorphic architectures were produced using PMTs composed of poly(ethylene oxide-*b*-hexyl acrylate) (Supporting Information Figure S1) dispersed in EtOH/HCl (aq.). A material precursor (niobium ethoxide) was added in various proportions to determine the material:template (M:T) ratio. For PMT conditions, the M:T ratio directly determines the wall thickness while maintaining a constant template/pore diameter. The resulting sample series were heated to different calcination temperatures to adjust the extent of amorphization while removing the polymer micelles and producing porosity. Scanning electron microscope (SEM) images are shown for a series of samples in Figure 1 with M:T = 1.2–3.0 and calcination temperatures from 520–600 °C. The samples are named using these two attributes in sequence (e.g., MT1.2–520 °C) and a consistent color scheme is used throughout where the hue corresponds to the calcination temperature and the shade corresponds to the M:T ratio. The SEM images were all consistent with disordered packing of ~95 nm spherical pores (dark) with an average wall thickness (light) that ranged from ~45–80 nm, increasing with M:T ratio (Figure 2e and f). Small-angle X-ray scattering patterns from the samples exhibited 2–3 peaks with approximate q-ratios of 1:2:3, consistent with randomly packed spheres.[97] The main SAXS peak shifts to lower q-spacing with increasing M:T ratio, corresponding to the lattice expansion that is expected with PMT behavior (Figure 2a–c). The corresponding d-spacing ($2\pi/q^*$) trends were all well fitted using a PMT model (Equations S1–S3, Figure 2d). The resulting best-fit parameters are shown in SI Table S3 where the average pore size increased slightly with calcination temperature due to further densification of the wall material. This densification is associated with reduced extent of amorphization where for example, grain boundaries and vacancies are anticipated to be reduced in prevalence. Thus, several sample series with isomorphic architectures were prepared with independent variation of wall thickness and nearly independent variation of amorphization extent.

The extent of amorphization was characterized by X-ray scattering, X-ray adsorption spectroscopy, X-ray photoelectron spectroscopy (XPS), and electron paramagnetic resonance (EPR). Grazing-incidence wide-angle X-ray scattering (GIWAXS)
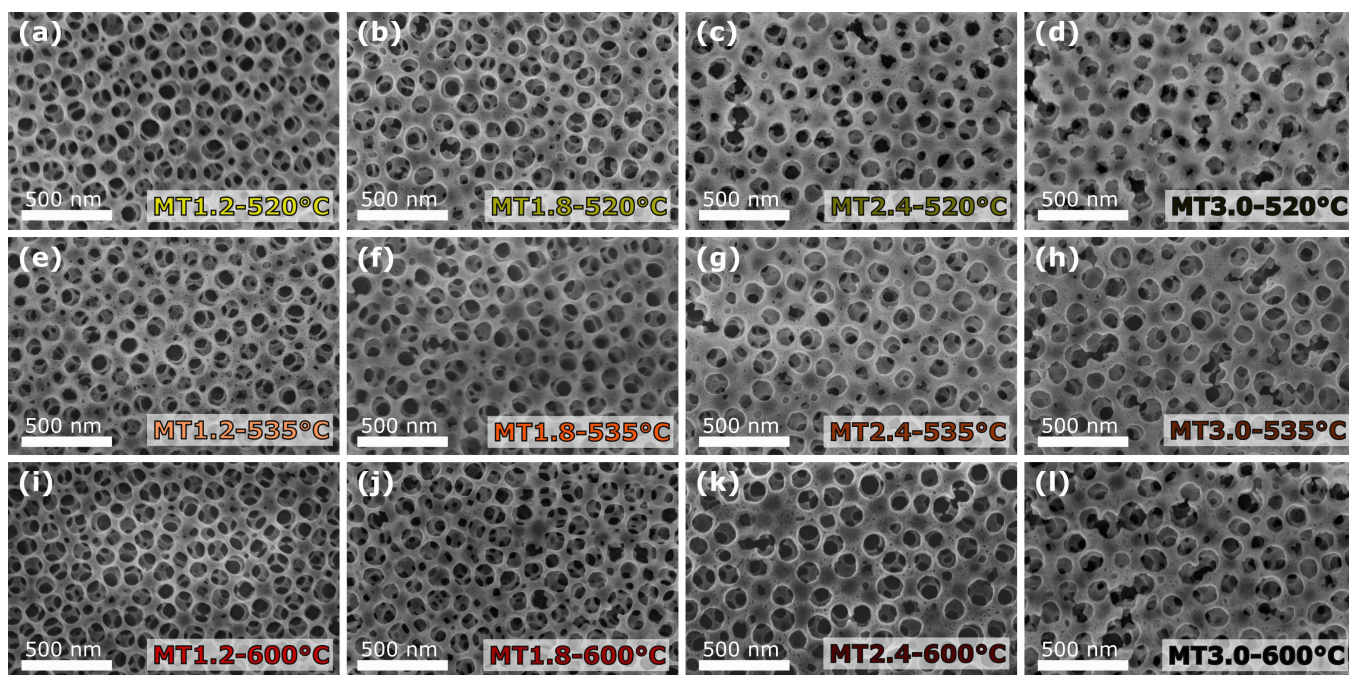
Figure 1. SEM images of the isomorphic series of porous niobia samples prepared with persistent micelle templates using different material:template (M:T) ratios and different calcination temperatures. The M:T ratios and calcination temperatures are noted in each panel. Subsequent figures preserve this color scheme with the hue corresponding to the calcination temperature and the shade corresponding to the M:T ratio.
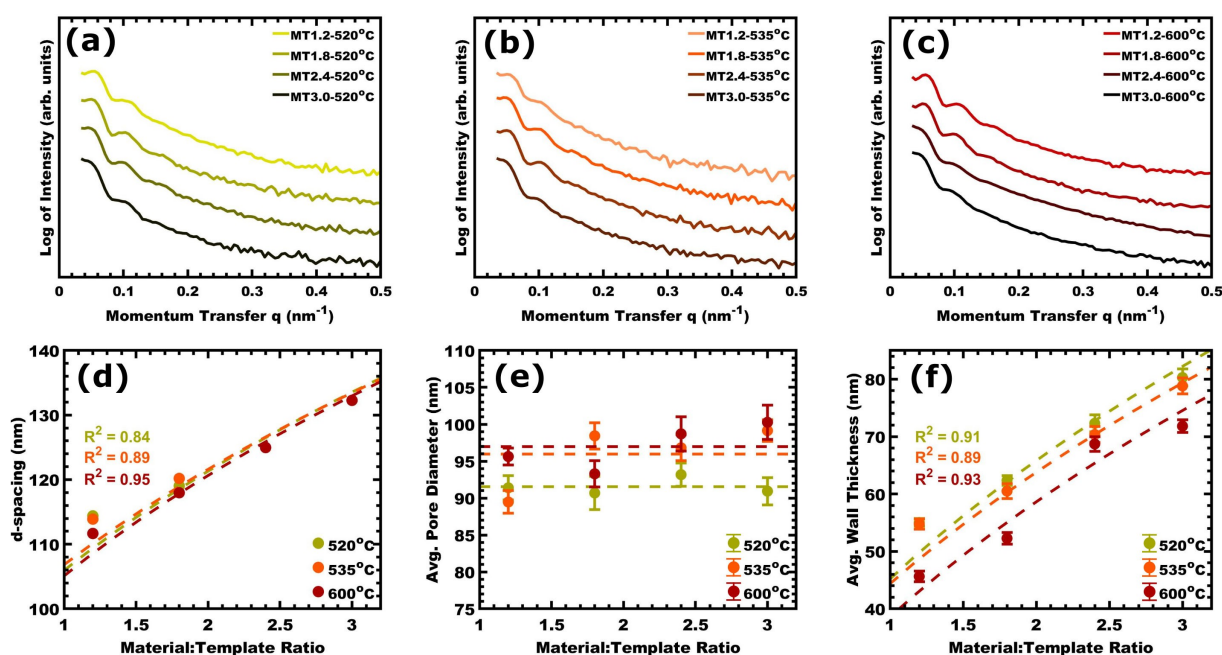

Figure 2. a–c) SAXS patterns for all samples from the isomorphic series arranged by calcination temperature: a) 520 °C, b) 535 °C, c) 600 °C. SAXS data were offset vertically for clarity. d) The corresponding d-spacing ($2\pi/q*$) trends reveal lattice expansion upon increasing material-to-template ratio (M:T). e) The mean pore diameters and f) mean wall thicknesses were determined from numerous measurements upon SEM images. d–f) Each of these metrics were compared to the PMT model (dashed lines) with goodness-of-fit (R^2) indicated. Values presented as mean ± standard error-of-the-mean.

patterns for fixed M:T = 1.8 and calcination temperature ranging from 475–600 °C are shown in Figure 3(a). Whereas MT1.8-475 °C was largely amorphous in character, the samples with higher calcination temperatures exhibited a series of peaks consistent with the orthorhombic T-Nb₂O₅. The peaks generally were narrower with higher temperature calcination. Scherrer analysis quantified the average crystallite size (without considering strain effects) where e.g., the samples with M:T = 1.8 exhibited an increasing average crystallite size trend of 12.8, 13.7, 13.5, 13.9, and 14.3 nm when calcined at 500, 520, 535,
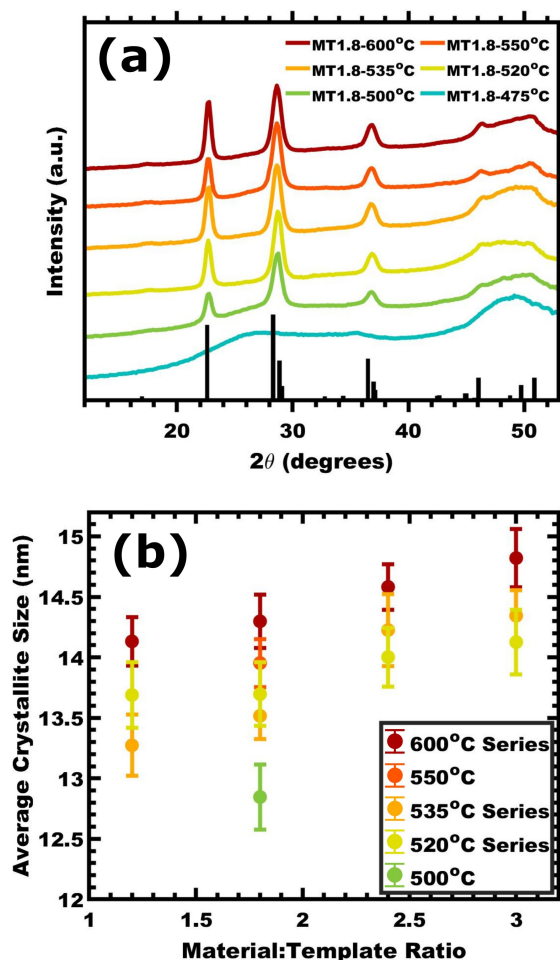
Batteries & Supercaps

Research Article
doi.org/10.1002/batt.202200056

Chemistry
Europe

European Chemical
Societies Publishing

Figure 3. a) GI-WAXS patterns for samples calcined at temperatures ranging from 475–600°C with constant M:T = 1.8. Data were offset vertically for clarity and include a T-Nb₂O₅ reference pattern (PDF No. 01-071-0336, black bars). b) The average crystallite size was calculated using Scherrer analysis of the non-convoluted (001) peak at 22.6° for different sample conditions. Values in panel (b) are presented as the mean ± standard error-of-the-mean.

550, and 600°C, respectively (Figure 3b). Such growth of progressively larger crystals can be accomplished either by the crystallization of amorphous regions or by Ostwald ripening of existing crystals. There was also an overall trend of increasing crystallite size with M:T ratio (increasing wall thickness). These observations indicate, as expected, that calcination promotes crystallization where the highest extent of amorphization occurs with the lowest calcination temperatures. Extended X-ray absorption fine structure (EXAFS) measurements were acquired near the Nb K-edge for samples spanning M:T = 1.2–3.0 and calcination temperatures spanning 300–600°C (Figure S2a). The k^2-weighted Fourier transform of $\chi(k)$ data exhibited known[20,98–100] Nb–O and Nb–Nb peaks with atomic distances at ~0.8–2 Å and ~2.4–4 Å, respectively (Figure 4c). Sample changes were compared using linear combination analysis (LCA) between the calcination endpoints of 300°C (most amorphous) and 600°C (most crystalline). The k^2-weighted $\chi(k)$ EXAFS data were similar within most M:T conditions (Figure S2a) thus the corresponding average decon-

volutions (crystalline vs amorphous) were compared. The resulting Figure 4(f) reveals a sigmoidal transition for niobia from amorphous to crystalline character that onsets around 500°C, similar to the GIWAXS trend, and the majority of samples were adequately fitted with two endpoint components. A few samples had significant residuals when fitted using these two components, where principle component analysis identified a third unknown component in these cases. The third component was not consistent with either pseudo-hexagonal TT-Nb₂O₅ nor T-Nb₂O₅ prepared via solid state synthesis[24] (Figure S2b) with the former standard having negligible contribution to additional LCA analysis (Table S4). The third component could perhaps be a distinct amorphous motif, but its further study is beyond the scope of this manuscript. Analysis of niobia crystal structures remains complex with multiple Nb-sites, partial occupancies, and a diversity of similar phases with minor differences in diffraction patterns.[99,100] XPS spectra were acquired on samples spanning from 520–600°C (Figure 4a and b). One notable feature was the gradual decrease in Nb 3d$_{5/2}$ energy with increasing calcination temperature. A recent XPS study identified a similar shift in the Nb 3d$_{5/2}$ peak location upon a calcination induced amorphous-crystalline transition, attributed to the addition of oxygen vacancies. In that report the amorphous phase Nb 3d$_{5/2}$ peak appeared at 207.46 eV whereas the corresponding T-Nb₂O₅ peak was at 206.98 eV.[101,102] These reference positions were used to estimate the amorphous and crystalline content of PMT films. This analysis (Figure 4e) suggests an increase in crystalline content from 68.4% ± 3.2% to 86.4% ± 1.7% for calcination at 520 to 600°C, respectively, similar to the EXAFS analysis. The O 1s region is often interpreted as a convolution of lattice oxygen, non-lattice oxygen, and H₂O or OH species with corresponding energies of 530.0, 531.2, and 532.6 eV, respectively (Figure 4a). The quantitative O/Nb composition, excluding non-lattice and hydrous species contributions, decreased from 3.96 to 2.13 with increasing calcination temperature, indicating progressive removal of O (Figure 4d). The implied sample stoichiometries of Nb₂O$_{4.3–8.0}$ were unexpected. The XPS calibration was validated using both commercial Nb₂O₅, NbO₂, and a T-Nb₂O₅ reference sample prepared by solid-state synthesis, the standard error of which was ±5% of the expected lattice-O/Nb stoichiometry. Assuming an upper limit oxidation state of Nb⁵⁺, this stoichiometry suggests a significant presence of oxygen in forms other than oxide O²⁻, such as interstitial O⁰, electron deficient oxygen anion O⁻, superoxide anion O₂⁻, peroxide anion O₂²⁻, or ozonide anion O³⁻. Several reports have claimed interstitial Oˣ species in diverse metal oxides,[103–107] however related XPS observations noted those between the lattice O peak and non-lattice O peak.[104–106] EPR analysis of samples calcined between 475–600°C were conducted to detect paramagnetic oxygen species containing unpaired electrons. The resulting spectra did not exhibit detectable signal associated with any paramagnetic oxygen species nor oxygen vacancies (Figure S3).[64,108–112] This observation suggests an absence of the considered paramagnetic oxygen species (O⁻, O₂⁻, O³⁻) where the combination of XPS and EPR is most consistent with oxygen present dominantly as
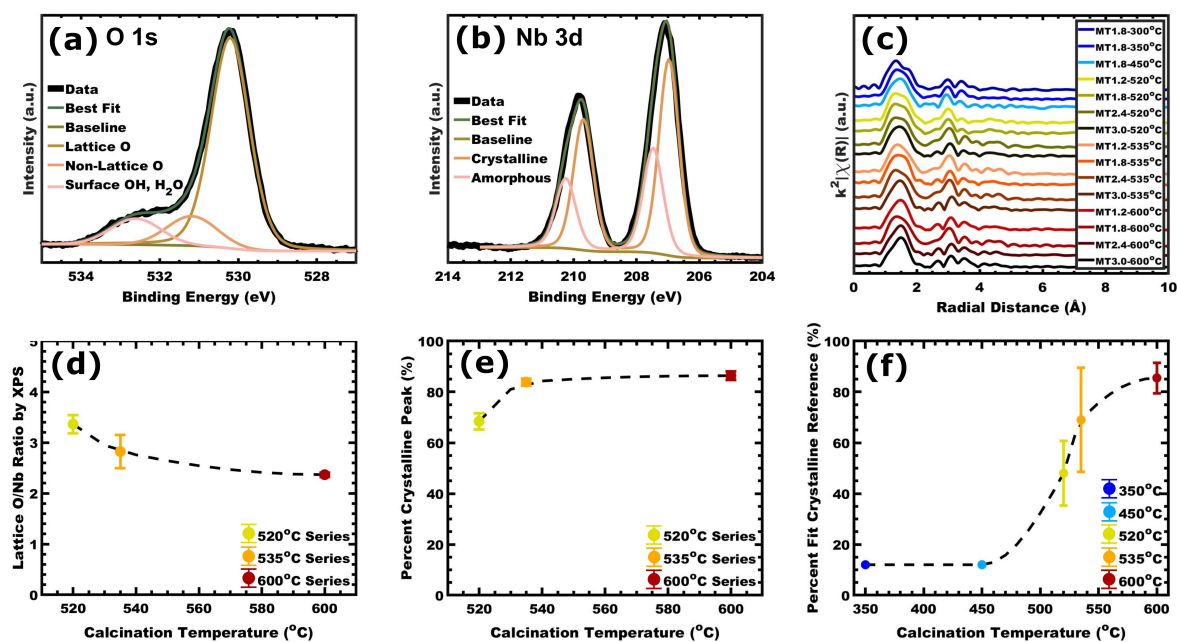
Batteries & Supercaps

Research Article
doi.org/10.1002/batt.202200056

Chemistry Europe
European Chemical
Societies Publishing

Figure 4. Representative XPS data from MT1.2-520 °C with showing the a) O 1s and b) Nb 3d regions. The oxygen peaks were termed as lattice (530.1 eV), non-lattice (531.1 eV), or surface OH/H_2O (532.5 eV). The Nb peaks were deconvolved as amorphous (210.28, 207.46 eV) and crystalline (209.68, 206.98 eV) contributions based on prior work. c) The EXAFS data are presented as k^2-weighted Fourier-transformed Nb K-edge. d) The XPS derived O/Nb ratio and the e) crystalline/amorphous ratio are shown. f) The EXAFS data were analyzed through a linear combination of MT1.8–300 °C as the amorphous references and MT2.4–600 °C as the crystalline reference to derive the percent crystallinity. Values presented with error bars represent the mean ± standard error-of-the-mean.

diamagnetic species, including oxide O^{2-}, hydroxide OH^-, and peroxide O_2^{2-} which are not observable by EPR. Density functional theory (DFT) calculations were performed on the O-rich niobia surface to better understand the excess oxygen configurations observed with low calcination temperatures (Figure S4), assuming that excess oxygen is likely to be located in the near-surface region. The DFT calculation revealed two different types of O—O bonds on the relaxed (001) surface as shown in Figure S4. The computed O—O bond distance in O_{po1} and O_{po2} is 1.44 and 1.39 Å, respectively, suggesting that both O_{po1} and O_{po2} are peroxide (O_2^{2-}). Prediction of energetically favorable peroxide formation on the relaxed O-rich surface is consistent with the measurements indicating excess diamagnetic oxygen species. Thus, the combination of experimental and DFT suggest that the amorphous niobia may be rich in peroxide defects that are gradually removed with increasing calcination temperature. Several changes to both the composition and atomic structure of orthorhombic niobia were found to vary with calcination temperature.

The cyclic voltammetry (CV) methods used to characterize the electrochemical behavior associated with each calcination temperature. The general approach is first described using a representative sample (MT1.2–600 °C) before comparing samples. A fixed voltage window from 1.2 to 3.0 V was scanned using series of voltage sweep rates (v) ranging from 3.2 to 1,000 mV s^{-1} and the current (i) response was recorded with a three-electrode configuration (Figure 5a). The resulting CV curves were characteristic of pseudocapacitance[10,113] with broad peaks having a box-like shape with narrow separation between anodic and cathodic peaks (see normalized data

Figure S5d–f). The anodic peaks were apparent for all v's investigated however the cathodic peaks became unobservable beyond 199.5 mV s^{-1} due to ohmic shift outside of the voltage window. The trends in anodic peak current are shown in Figure 5(b). A power law relationship[114] is often used to identify the type of rate-limiting process:

$$i = av^b \tag{1}$$

where i is peak current, and a and b ("b-value") are fit terms. Surface-limited behavior such as ideal capacitance exhibit $i \propto v$ (b = 1.0) whereas semi-infinite diffusion-limited behavior exhibits $i \propto v^{0.5}$ (b = 0.5). The anodic i(v) is shown in Figure 5(b) on a log-log scale where the slope corresponds to the b-value. The derivative of Figure 5(b) is shown as a plot of b-value(v) in Figure 5(c). Here MT1.2–600 °C exhibits a b-value > 0.9 for $v \leq$ 87.1 mV s^{-1}, indicative of surface-limited behavior, i.e., pseudocapacitance. The departure from surface-limited kinetics with increasing v-values was previously termed the surface limited threshold (SLT, v_{SLT}, t_{SLT}) defined as b = 0.9.[21] Please note that b-values that are non-proximal to 1.0 and 0.5 are ambiguous to interpret due to the convolution of multiple rate-limiting processes. Thus, the SLT represents the point where diffusion-limited processes become apparent. Condition MT1.2–600 °C had $v_{SLT} = 87.1 \pm 0.3$ mV s^{-1}, corresponding to a charge time (t_{SLT}) of 20.66 ± 0.08 s. For the samples investigated here, the v_{SLT} also corresponds to the onset of diffusion-limited capacity loss (Figure S6). This methodology thus identifies the transitions in type of rate limiting process where further comparisons are needed to identify the specific diffusive process.
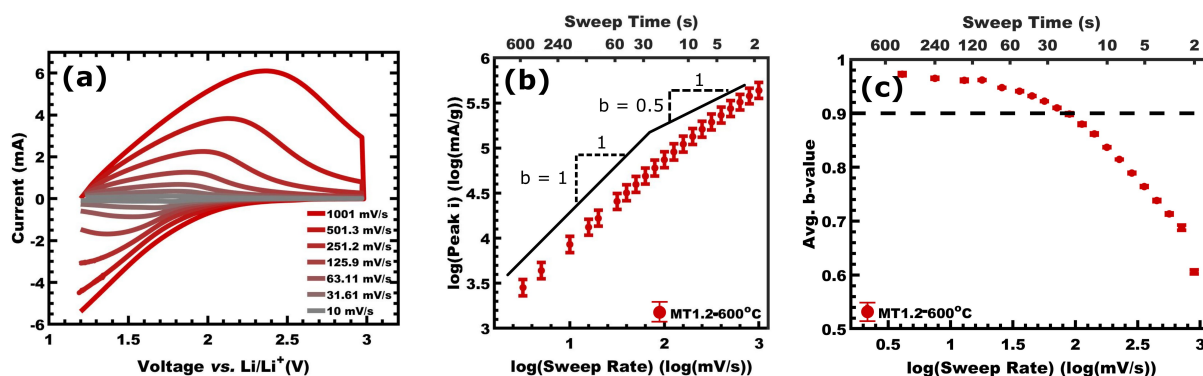
Batteries & Supercaps

Research Article
doi.org/10.1002/batt.202200056

Chemistry Europe
European Chemical
Societies Publishing

Figure 5. a) Representative cyclic voltammograms at different voltage sweep rates for sample MT1.2-600 °C at different voltage sweep rates. b) A log-log plot of anodic, mass-normalized peak current vs. voltage sweep rate. The slope (*b*-value) of this log-log plot identifies the type of rate limiting process. c) The corresponding derivative shows b-value changes with the voltage sweep-rate. The surface-limited threshold (SLT) denotes the departure from surface-limited kinetics ($b = 0.9$, dashed line). Values are presented as mean ± standard error-of-the-mean.

This kinetic analysis combined with controlled experiments were used to interpret the specific diffusive process that limits the v_{SLT} for each temperature series. First the 520 °C series is elaborated before turning attention to the other calcination temperatures. Four samples spanning M:T = 1.2–3.0 were compared with similar film thicknesses (Figures 6a and b, S6, S7, and Tables S5 and S6,). Performance changes may be associated with changes to the surface-limited process, the diffusion-limited process(es), or some combination thereof. Thus, the analytical strategy examines both possible changes. For the 520 °C series, the peak currents at $v = 3.2$ mV s^{-1} were varied less than the error of the measurement, not indicating a marked change in the rate of the surface-limited process with M:T. With respect to the diffusion-limited processes, the *b*-value(v) trends were compared where $v > v_{SLT}$ contains diffusion-limited contributions of varying magnitudes. For these samples the v_{SLT} monotonically shifted to higher v with lower M:T (Figure 6b). For example, MT1.2–520 °C and sample MT3.0-520 °C exhibited v_{SLT} values of 136.3 ± 2.1 and 56.0 ± 0.5 mV s^{-1}, respectively. This 143 % increase is quite large for a 25.5 nm (33.8 %) reduction in wall thickness. These data alone, however, are not yet definitive towards a specific diffusive process. For example, the increase of wall thickness is geometrically coupled to a decrease in the pore volume fraction which will decrease the effective conductivity of the electrolyte phase. To check for this constraint sample MT3.0-520 °C with the thickest walls and lowest volume fraction of porosity was examined with an electrolyte of half the prior concentration. The 50 % decrease in electrolyte concentration was found to have no marked effect upon the peak current nor *b*-value(v), indicating that electrolyte transport was not rate limiting for these samples (Figure 6e). For due diligence, the sensitivity of the architecture towards film thickness was next investigated which affects both electrolyte and electron transport. Having previously excluded sensitivity towards electrolyte constraints, differences here should be attributed to electron transport alone. Samples of MT3.0-520 °C were compared to samples of MT3.0-520 °C-Thick which had the film thickness increased from 65.2 to 163.0 nm, a ~150 % increase. The corresponding peak currents found a

2.6 % decrease however, the b-value(v) plots revealed some effect of film thickness with the v_{SLT} shifting from 56.0 ± 0.5 to 40.6 ± 0.3 mV s^{-1}, a 28 % decrease (Figure 6h, Figure 7a). Thus, the minor restriction from electron transport and minor changes in overall sample thickness with M:T do not explain the significant 143 % increase in v_{SLT} found with decreasing M:T conditions with similar thicknesses (SI Table S6). Thus, by the process of elimination one can conclude that dominant diffusion-limited process at v_{SLT} is solid-state lithium intercalation with a minor contribution from electron transport. The other calcination temperature series at 535 °C and 600 °C exhibited similar trends overall including: 1) similar peak currents (mA g^{-1}) with changing M:T ratio (Figure 6a); 2) a shift in *b*-value(v) corresponding to increasing v_{SLT} with decreasing M:T ratio (Figure 6c and d); 3) no significant change in peak current nor v_{SLT} with changing the electrolyte concentration from 1.0 M to 0.5 M (Figure 6f and g); and 4) a minor reduction of peak current and a ~28 % decrease in v_{SLT} with increased film thickness (Figure 6i and j). Thus, all sample series calcined from 520–600 °C were concluded to have solid-state lithium diffusion as the dominant diffusive constraint and are further analyzed with diverse models (*vide infra*). Figure 7(a) presents the corresponding t_{SLT} values (t_{SLT} = voltage window ÷ v_{SLT}) showing how both thinner walls from lower M:T ratios and lower calcination temperatures both lead to faster t_{SLT} times, ranging from ~13–35 s. Despite the onset of a diffusive contribution for $v > v_{SLT}$, the samples retain excellent rate-capability (Figure 7b). For example, MT1.2-520 °C maintained 95 % of its capacity (577.4 ± 17.0 C g^{-1}) with a sweep time of 2.25 s (1600 C-rate equivalent) exceeding many literature precedents for T-Nb$_2$O$_5$. Furthermore, many of these comparison reports included conductive additives for particle-based slurries (typically not included in mass-normalization),[115,116] whereas our thin films were purely composed of niobia. The limits to amorphization of orthorhombic niobia are next discussed with a larger temperature range.

The electrochemical behavior of lower calcination temperatures was examined down to 300 °C. The CV curves for samples from 300–500 °C exhibited profiles that were consid-
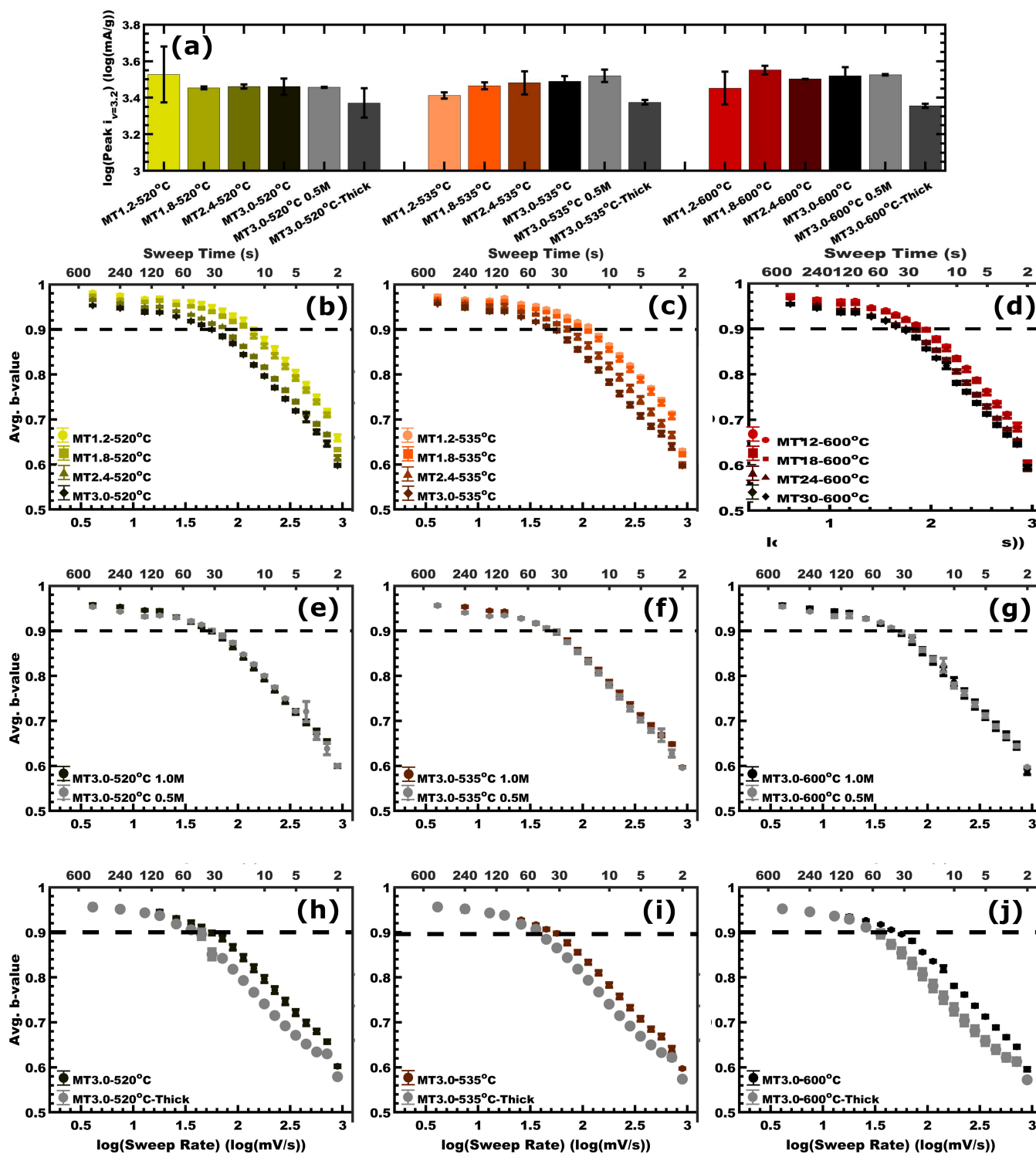
Figure 6. Examination of possible kinetic constraints from the intercalation length, electrolyte transport, and electron transport for a range of samples with calcination temperatures of 520 °C, 535 °C, and 600 °C. Comparisons include a) the peak current at $v = 3.2$ mVs^{-1}, b–d) b-value(v) with wall thickness (M:T ratio), e and f) b-value(v) with 1.0 M vs. 0.5 M electrolyte, h and i) b-value(v) with standard thickness (~75 nm) vs. thicker films (~120% thicker). Values are presented as the mean ± standard error-of-the-mean.

erably broader, spanning a larger voltage range, than T-Nb$_2$O$_5$ similar to prior reports of amorphous niobia (Figure 8a).[19,22,24,25,62,71] Curiously this CV peak breadth increased somewhat with calcination temperature up to a maximum width at 500 °C, corresponding to the GIWAXS onset of

crystallization (Figure 3), then substantially narrowing with further increasing calcination temperature. This CV trend suggests increasing charge localization as crystalline samples are heated at higher calcination temperatures,[10] i.e., increasing delocalization with T-Nb$_2$O$_5$ amorphization. The CV-character as
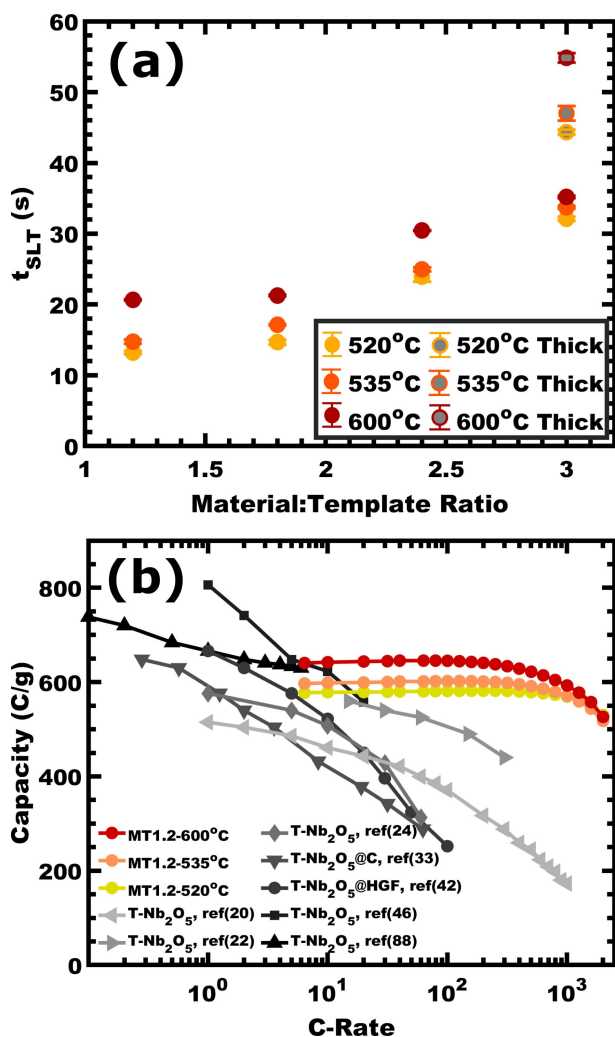
Figure 7. a) Comparison of the CV sweep times corresponding to the surface-limited threshold (t_{SLT}) for all sample conditions presented thus far. Values are presented as the mean $\pm$ standard error-of-the-mean. b) The rate-dependent lithiation capacity of MT1.2-520°C is compared to published precedents as a function of C-rate or effective C-rate.

Figure 8. a) Comparison of normalized CV data for wide range of calcination temperatures with constant MT = 1.8 measured at $v = 3.2$ mV s^{-1}. b) Comparison of the corresponding normalized charge with repeated electrochemical cycling at 10 mV s^{-1} reveals that samples calcined at 500°C or below are unstable. Values are presented as mean $\pm$ standard error-of-the-mean.

well as the GIWAXS, EXAFS, and XPS trends were clustered into two groups, the mostly-amorphous samples calcined between 300–475 °C and the mostly-crystalline samples calcined between 520–600 °C. Whereas the mostly-crystalline samples exhibited reproducible lithiation capacity upon cycling, the mostly-amorphous samples all exhibited a marked ~30%–40% decline in lithiation capacity (Figure 8b) and were thus only briefly examined. Having noted the limited stability of mostly-amorphous samples, their electrochemical kinetics were examined as described before. As shown in Figure 9(a), there was an increase in low-v peak currents with increasing calcination temperature, suggesting an accelerated surface reaction rate (*vide infra*). While comparisons among the mostly-crystalline samples and the mostly-amorphous samples are both consistent with this trend, caution should be taken in comparing the end points since the CV curve shapes simultaneously varied which alters the peak current values. The *b*-value(v) data for a set of samples with M:T = 1.8 are presented spanning all
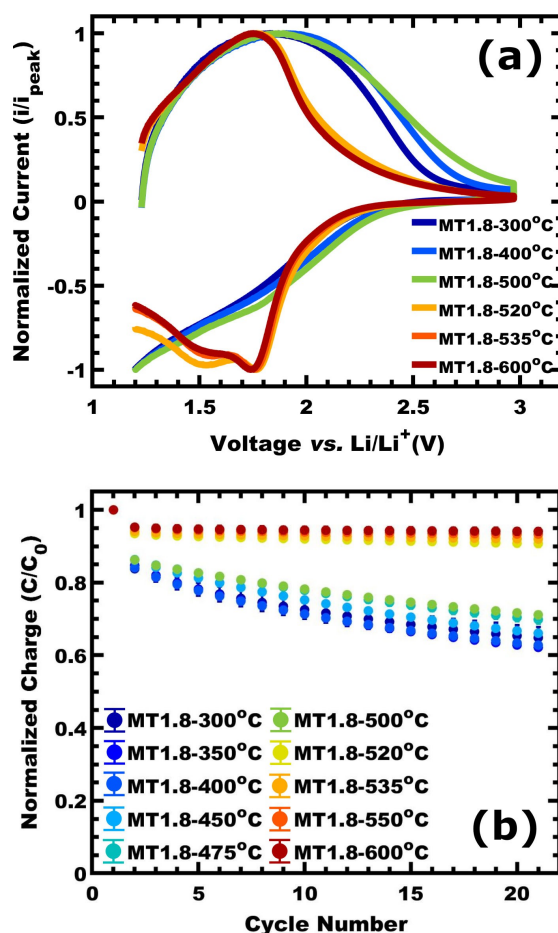
calcination temperatures investigated here (Figure 9b). Again, the mostly-amorphous and mostly-crystalline samples clustered into two distinct groups with the mostly-amorphous samples exhibiting the highest v_{SLT} values. The corresponding t_{SLT} value exhibited a sigmoidal trend with the fastest time found for the mostly-amorphous samples (Figure 9b). The most interesting region of this amorphization continuum is the 520–600 °C samples that were mostly-crystalline, electrochemically stable, and revealed monotonic kinetics changes (Figure 9b and c). A general increase in lithiation capacity was noted with increased calcination temperature with average values (all M:T ratios) of 625.8 $\pm$ 29.7 C g^{-1} at 520 °C, 669.7 $\pm$ 47.8 C g^{-1} at 535 °C, 727.5 $\pm$ 60.9 C g^{-1} at 600 °C (SI Figure S6) approaching the theoretical capacity of 726 C g^{-1} for Li$_2$Nb$_2$O$_5$.[117] Thus the mostly-crystalline samples (520–600 °C) were found to have the most compelling collection of attributes including stable lithiation capacity and adjustable kinetics via calcination temperature.

Further insights into the differences in electrochemical kinetics were elucidated with a simple current model. As noted above, the SLT reflects the tipping point from surface-limited kinetics towards a convolution that includes diffusion-limited
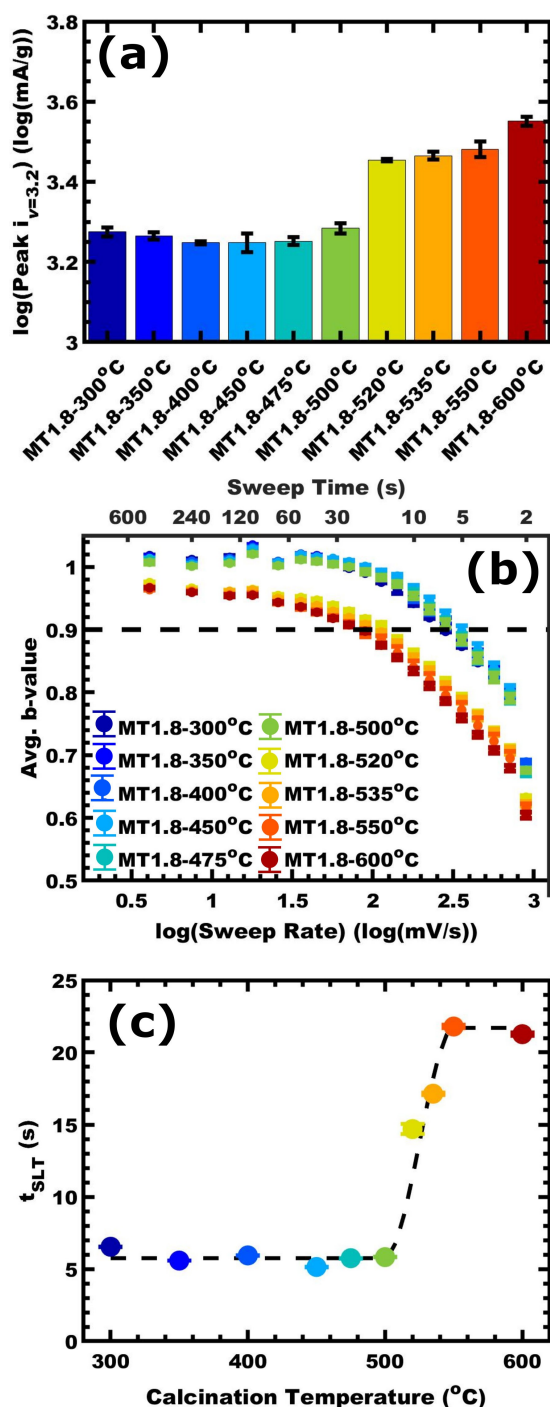
Figure 9. Comparisons of electrochemical kinetics for initial measurements on MT $= 1.8$ samples with calcination temperatures ranging from 300 °C to 600 °C. Comparisons include a) the peak current at $v = 3.2$ mV s^{-1}, b) b-value(v), c) and sweep times at the corresponding surface-limited thresholds (t_{SLT}). Values are presented as mean $\pm$ standard error-of-the-mean.

contributions where increases in v_{SLT} could in principle be attributed to either a decrease in the surface-limited reaction rate or an increase in the diffusion-limited reaction rate. A popular model was developed for $i(v)$ surface-redox pseudocapacitive materials[118] where surface-limited and diffusion-limited contributions were parametrized with:

$$i = k_1 v + k_2 v^{0.5} \tag{2}$$

where k_1 and k_2 are fit parameters that are analogous to admittance (larger k values lead to larger current). This expression includes two separate sources of current that operate in parallel and are added together (termed here "parallel model"). This parallel model includes a surface-limited current from the charging of the "near surface" material and a separate diffusion-limited current from the rest of the material. The corresponding theoretical plot on a log-log scale shows how the dashed lines for k_1-alone and k_2-alone add together to yield the total current (Figure 10a). This functional form fundamentally transitions from diffusion-limited behavior at low v to surface-limited behavior at high v (Figure 10a). That trend is most apparent by examining the corresponding derivative i.e., b-value(v) for the parallel model (Figure 10c). This behavior trend however does not match the experimental data here. A revised perspective is proposed where both a surface-limited process and a diffusion-limited process operate in series, here termed the "series model" [Derivation in SI Equations S(4)–S(10) with $R = 0$]:

$$i = \left[\left(\frac{k_2}{\sqrt{v}} \right)^2 + \left(\frac{k_1}{v} + \frac{k_2}{\sqrt{v}} \right)^2 \right]^{-0.5} \tag{3}$$

where k_1 and k_2 are fit parameters that are analogous to impedance (lower values lead to higher currents). Notably the k_1 term corresponds to the impedance of a surface-limited process and the k_2 term corresponds to the impedance of a diffusion-limited process. The corresponding theoretical plot on a log-log scale shows how the total current remains below both the k_1-alone and k_2-alone contributions (dashed lines), reflecting that both processes restrict current (Figure 10b). In contrast to the parallel model, the series model thus fundamentally transitions from surface-limited behavior to diffusion-limited behavior with increasing v. Again, the corresponding derivative reveals a b-value(v) trend (Figure 10d) which closely matches the samples investigated here (compare to Figure 6). Notably, the series model does not presume the existence of a special near-surface region[10] and does not assume that the diffusion-limited current operates in the absence of a surface-limited contribution (consider Occam's razor). Thus, a series model for current is proposed to quantify surface and diffusion contributions which matches experimental observations.

The utility of these models is compared with one dataset. The M:T $= 1.2$ series calcined at 520, 535, and 600 °C are presented as $i(v)$ and b-value(v) in Figure 11 using best fits from each model. Since the log-log plot of $i(v)$ is mostly linear, both models yield an excellent fit in this coordinate space with goodness-of-fit R^2 values > 0.99 (Figure 11a and b). In contrast, the parallel model is unable to track the general shape of b-value(v) due to its functional form, *vide supra*, giving very poor fits with goodness-of-fit $R^2 \leq -1.1$ (Figure 11d). Given the poor congruence between the parallel model and b-value(v) observations, it is questionable how much faith should be put to its use to separate surface-limited and diffusion-limited capacities.

Batteries & Supercaps

Research Article
doi.org/10.1002/batt.202200056

Chemistry Europe
European Chemical
Societies Publishing

$$I = k_1\nu + k_2\sqrt{\nu}$$

$$I = \left[\left(\frac{k_2}{\sqrt{\nu}}\right)^2 + \left(\frac{k_1}{\nu} + \frac{k_2}{\sqrt{\nu}}\right)^2\right]^{-0.5}$$
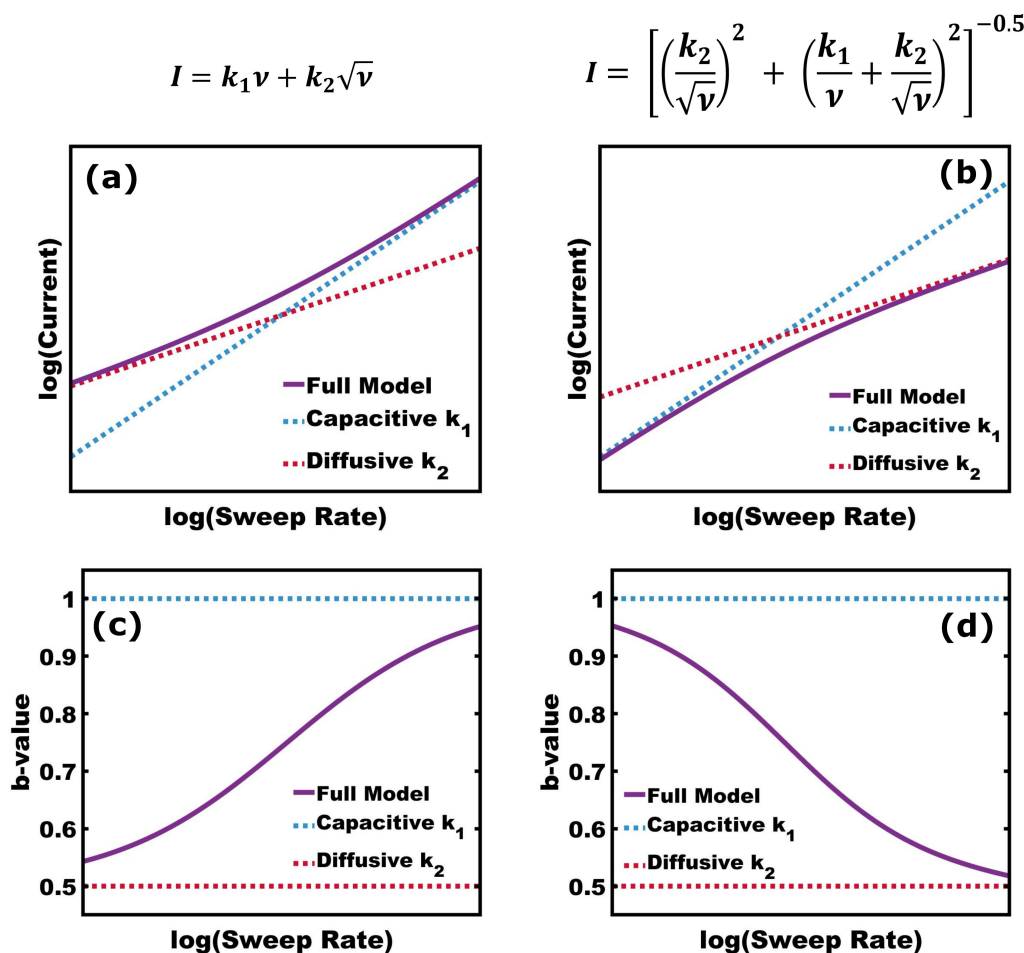

Figure 10. Comparison of current models as a function of voltage sweep rate with surface-limited and diffusion-limited elements connected in either a) parallel or b) series. c and d) The corresponding derivative plots present *b*-value(ν) which identify the type of the dominant rate-limiting process as surface-limited ($b \sim 1.0$), semi-infinite diffusion-limited ($b \sim 0.5$), or a mixture thereof.

The series model, on the other hand, closely matches experimental *b*-value(ν) trends for all samples with goodness-of-fit $R^2 \geq 0.82$ (Figure 11e). The addition of a single additional fit term corresponding to a series resistor improved the goodness-of-fit for *b*-value(ν) with $R^2 \geq 0.98$ for these samples (Figure 11c and f). Several modifications were examined, including implementation of a constant phase element, inclusion of a second diffusion-limited process, and the addition of a resistor term were examined where the latter was selected due to the improved fit. In the interest of matching data trends with minimal complexity the series model was limited to three terms here where [Derivation in Equations S-(4)–S(10) with $R \neq 0$]:

$$i = \left[\left(\frac{k_2}{\sqrt{\nu}} + R\right)^2 + \left(\frac{k_1}{\nu} + \frac{k_2}{\sqrt{\nu}}\right)^2\right]^{-0.5} \tag{4}$$

where R corresponds to the impedance of a resistor. The effects of a range of theoretical parameters upon $i(\nu)$ and *b*-value(ν) are presented in Figure S8. As expected, increasing the k_2 impedance reduces the $i(\nu)$ in the high-ν regime and similarly increasing the k_1 impedance reduces the $i(\nu)$ in the low-ν

regime (Figure S8a–d). A perhaps surprising feature is that the *b*-value(ν) trends and the implied ν_{SLT} depend largely on the ratio of k_1/k_2 (constant $R = 0$) despite significant changes in $i(\nu)$ performance (Figure S8e and f). Lastly the effect of increasing R is presented where $i(\nu)$ decreases and *b*-value(ν) exhibits increasing curvature and reaches *b*-values < 0.5 (Figure S8g and h). A notable advantage is that the use of either series model enables the independent assessment of the rates (impedances) of the surface-limited and the diffusion-limited processes.

The best-fits of the series model [Equation (4)] were compared to quantify changes to rates of surface and diffusion processes across many sample conditions. Samples spanning M:T = 1.2—3.0 and calcination temperatures 520—600 °C were all well-fitted in the $i(\nu)$ coordinate space with the corresponding *b*-value(ν) plots included for comparison (Figure S9). Figure 12 shows the trends for best-fit parameters k_1, k_2, and R as a function of the calcination temperature (different colors) and the intercalation length (horizontal axis, half the wall thickness). Please note all current data was mass-normalized before fitting. Starting with the surface process the k_1 impedance decreases (faster surface process) with increasing calcination temperature.

Batteries & Supercaps

Research Article
doi.org/10.1002/batt.202200056

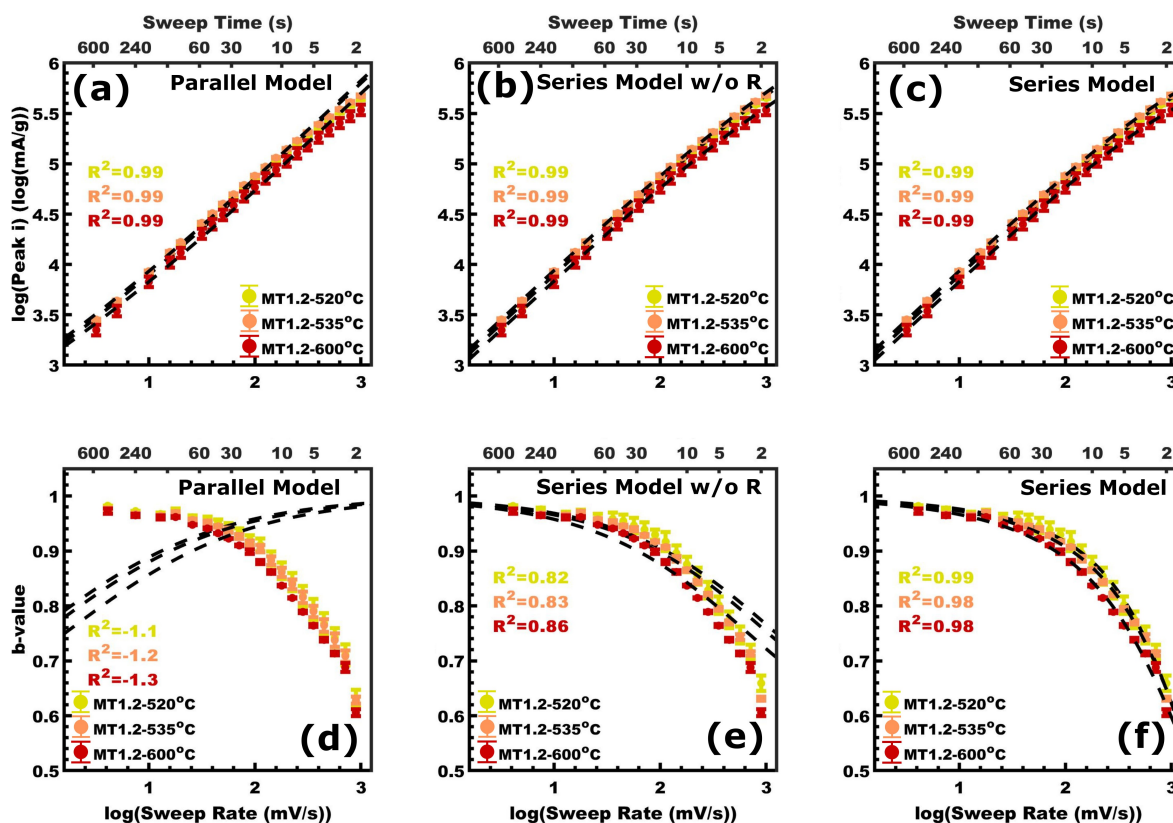**Chemistry Europe**
European Chemical
Societies Publishing

Figure 11. Comparison of three current models where the best-fits had similar goodness-of-fit values $R^2 > 0.99$ for a) the parallel model, b) the series model without a resistor, and c) the series model with a resistor. d–f) The corresponding derivatives show b-value(v) relative to each model where only the series models are similar to the data. f) The resistor addition to the series model improves the goodness-of-fit $R^2 \geq 0.98$ for all three sample conditions. Values are presented as mean $\pm$ standard error-of-the-mean.

The accelerated surface process with calcination temperature may be associated with the increased extent of crystallization, or the removal of defects associated with excess oxygen noted by XPS. For example, interstitial oxygen species could act as an additional Li–O coordination motif which have been calculated to increase the energy for lithium adsorption.[23] Within each temperature series, the k_1 impedance generally decreased (faster surface process) with increasing wall thickness despite the naturally accompanying decrease in mass-normalized surface area (Figure 12a). This trend may be associated with the increased crystallite size found with thicker walls (higher M:T) within each temperature series. The implied trends for a faster surface process with increasing M:T, however, were not apparent when comparing the individual low-v peak current values for each temperature series, a small change that is perhaps better revealed by fitting each full $i(v)$ dataset. Second, the diffusive process k_2 impedance generally decreased (faster diffusion process) with lowered calcination temperatures. This is consistent with the prior discussion where solid state lithium diffusion was identified as the dominant diffusive process where lowering the calcination temperature was found to increase the rate of lithium diffusivity (Figure 12b, Table 1). Within each temperature series, the k_2 impedance generally increased with wall thickness (or M:T), likely associated with the increased diffusion length which fit reasonably to a linear

Table 1. Comparison of kinetic descriptors for sample series with different calcination temperatures.			
Sample Series	Slope of Figure 12(b) k_2 [((mV s^{-1})$^{0.5}$(mA g^{-1})$^{-1}$) nm^{-1}][a]	Slope of Figure 12(d) [(s)$^{0.5}$ nm^{-1}][a]	Average R value [(mA g^{-1})$^{-1}$][a]
520 °C Series	7.183E-7 (−12.17 %)	0.1342 (−21.34 %)	6.888E-7 (15.09 %)
535 °C Series	7.218E-7 (−11.74 %)	0.1425 (−16.47 %)	6.413E-7 (7.151 %)
600 °C Series	8.178E-7 (0 %)	0.1706 (0 %)	5.985E-7 (0 %)
[a] The percent change relative to the 600 °C Series is noted in parentheses			

trend. This diffusion-length kinetic dependence is also revealed for each temperature series in a plot of $t_{SLT}^{0.5}$ vs diffusion length where a straight line is expected for a 1D general solution (half concentration of source) to Fick's second law with an semi-infinite source[21] ($x \propto (Dt)^{0.5}$) (Figure 12d). The $t_{SLT}^{0.5}$ plot is also consistent with the diffusivity trend where decreasing calcination temperature led to lower slopes corresponding to faster t_{SLT} values and higher lithium diffusivity (Figure 12d). Thus, there is agreement upon this conclusion from both the t_{SLT} and the k_2 perspectives with an observed 21.34 % decrease, and 12.17 % decrease in slope of the 520 °C condition relative to the

Batteries & Supercaps

Research Article
doi.org/10.1002/batt.202200056

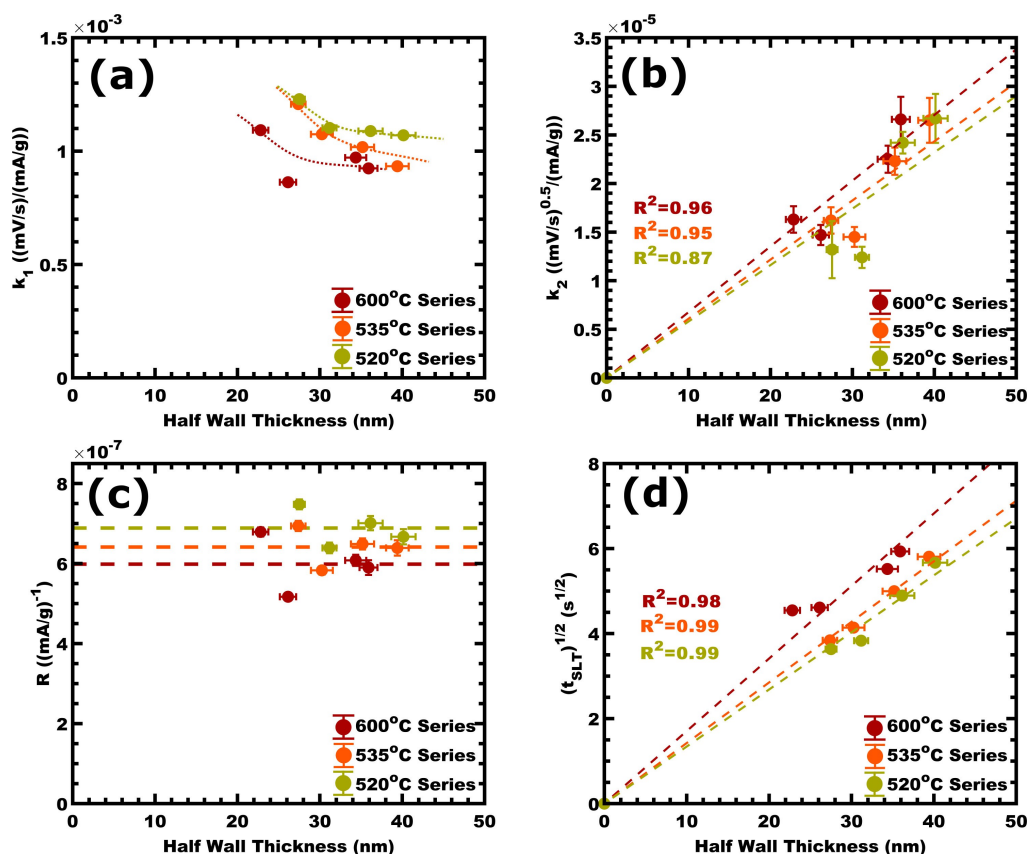**Chemistry Europe**
European Chemical
Societies Publishing

Figure 12. a–c) The peak currents for all sample conditions were fitted using the series-model and the best-fit parameters were compared as a function of half the wall thickness (intercalation pathlength). a) The k_1 term corresponds to the impedance of a surface-limited process with a dotted line to guide the eye. b) The k_2 term corresponds to the impedance of a diffusion-limited process with dashed lines corresponding to linear best-fits. c) The R term corresponds to a resistance with a dashed line to represent the average for each series. d) For comparison to b) $t_{SLT}^{0.5}$ is plotted vs the intercalation length where a linear trend is consistent with a generalized diffusion relationship from Fick's second law. Values are presented as mean ± standard error-of-the-mean.

600 °C condition, respectively (Figure 12b and d). Previous work comparing amorphous and crystalline metal oxide counterparts suggest lithium diffusivity is improved when amorphization lowers the energy barrier for lithium site hopping.[25,73,84,86,119—123] The granular kinetic changes resulting from variation of calcination temperature could be the result of an ensemble of phases or alternatively a granular change in the average local atomic environment. Lastly, the resistive impedance R was relatively constant for all samples with a minor reduction with increasing calcination temperature as observed in amorphized T-Nb_2O_5[64] or perhaps indicative of improved contact resistance between the niobia film and the FTO substrates (Figure 12c, Table 1) similar to that observed elsewhere when comparing anatase and amorphous TiO_2 films.[124] Thus the use of the series model to interpret lithiation kinetic changes provided evidence that decreasing the calcination temperature, i.e., increasing the extent of amorphization, both accelerates the solid-state diffusion of lithium ions and decelerates the surface reaction.

Conclusion

Amorphization provides an avenue to enhance diffusion rates for improved rate capability with intercalation pseudocapaci-

tance. The identification and quantification of such amorphization effects are challenging when the experimental samples contain multiple simultaneous variations. Here, PMTs enabled the production of niobia sample series with tunable isomorphic architectures calcined over a range of temperatures. Using GIWAXS, XAFS, XPS, and EPR, the degree of amorphization was found to increase with lower calcination temperatures and was consistent with increasing peroxide as supported by DFT calculations. While the mostly-amorphous samples were not stable to cyclic lithiation, the mostly-crystalline samples were stable and exhibited marked kinetic changes with calcination temperature. Through process of elimination and variation of a single transport parameter at a time, solid-state lithium diffusion was identified as the dominant diffusive process which limits v_{SLT}. A series model for $i(v)$ was proposed which closely matched experimental observations while simultaneously quantifying the impedance of the surface process and the dominant diffusion process. This series model revealed that amorphization led to a 12.2% decreased diffusion-limitation and a 17.0% increased surface-limitation amongst the stable samples. The use of isomorphic architectures that vary a single spatial parameter at a time uniquely support the disambiguation of fundamental kinetic processes. Lastly, these results reveal a new high-performance material which achieved 577 ±

Batteries & Supercaps

Research Article
doi.org/10.1002/batt.202200056

Chemistry Europe
European Chemical
Societies Publishing

17 C g^{-1} capacity (95% retention) with a 2.25 s response time, corresponding to an effective C-rate of 1600 C.

Experimental Section

Materials

Ethanol (EtOH 200 proof, 100%, Fisher) was stored over 30% w/v of molecular sieves (3 Å, 8–12 mesh, Acros Organics) for a week.[125] 2-bromopropionic acid (>99%, Aldrich), chloroform (>99%, Aldrich), dimethylformamide (97%, Aldrich), hexane (>98.5%, Fisher), concentrated hydrochloric acid (HCl, 37% w/w, ACS grade, VWR) and (HCl, 37% w/w, trace metal grade, Fisher Scientific), concentrated hydrofluoric acid (HF, 48% w/w, trace metal grade, Sigma-Aldrich), niobium(IV) oxide (>99%, metal basis, Alfa Aesar), concentrated nitric acid (HNO$_3$, 70%, Fisher Scientific), poly(ethylene glycol)methyl ether (PEO-OH, $M_n = 20,000$ g mol^{-1}, Aldrich), 4-(dimethylamino) pyridine (99%, Aldrich), tetrahydrofuran (Fisher, certified), and were used as received. Niobium(V) ethoxide (NbOEth, 99.9%, Fisher), copper(I) bromide (99.99%, Aldrich), tris-(2-dimethylaminoethyl) amine (97%, Aldrich), anhydrous lithium perchlorate (LiClO4, 99.99%, Aldrich), and anhydrous propylene carbonate (99.7%, Aldrich) were used as received and stored inside an argon-filled glove box. Hexyl acrylate (96%, VWR) monomer was passed through a basic alumina column just prior to use for polymerization.

Polymer synthesis

Poly(ethylene oxide-b-hexyl acrylate), PEO-b-PHA, diblock polymer was synthesized by a two-step synthesis. A Steglich esterification of poly(ethylene glycol)methyl ether synthesized the macroinitiator, followed by an atom transfer radical polymerization to create the PHA block. The synthesis is described elsewhere in detail.[89] The molar mass of PHA was determined using a Bruker Avance III HD 300 ^{1}H NMR by comparing it to the PEO methyl ether starting material ($M_n = 20.0$ kg mol^{-1}) (Figure S4a and Table S1). The molar mass dispersity was characterized using a Waters gel permeation chromatograph (GPC) equipped with a Waters 1525 binary pump, three styragel columns (HR1, HR3, HR5 in the effective molecular weight range of 0.1–5, 0.5–30, and 2–400 kg mol^{-1}, respectively), and a Waters 2414 refractive index detector with THF as the carrier solvent. The GPC was calibrated with poly(styrene) standards (1.50, 3.28, 10.00, 17.40, 32.70, 120.00, 214.00, 545.00, 1010.00 kg mol^{-1}) obtained from Polymer Standards Service GmbH. GPC samples were prepared in THF at concentrations of 5 mg mL^{-1}, filtered through a 0.2 µm PTFE syringe filter prior to injection (Figure S1b and Table S1).[90,126]

Synthesis of porous materials with persistent micelle templates

A micelle template stock solution was prepared by dispersing PEO-b-PHA (25 mg) in EtOH (2.5 mL) at 80 °C in a sealed 20 mL scintillation vial with a PTFE lined cap then allowed to cool to room temperature overnight. Concentrated HCl (37 wt%) (≈ 0.060 g) was added slowly to reach 1.8 wt% with respect to the total mixture (PEO-b-PHA, EtOH, and HCl). We note that ethanol was found to result in minimal microporosity within the final niobia walls.[93] After acid addition, the solution was placed in a water bath at 35 °C to maintain dispersion of the polymer micelles. A prescribed quantity of NbOEth was added to a 20 mL scintillation in an argon-filled glovebox (<1 ppm O$_2$, <1 ppm H$_2$O) and once removed from the glovebox was mixed with a prescribed amount of micelle template

solution via injection through PTFE lined cap to reach the target material-to-template ratio, M:T ratio.[89] Once mixed, the solution was placed back in the water bath. Here the M:T ratio is a mass ratio of the final anticipated niobia mass relative to the mass of block polymer. Each film was spin coated for 30 s at 1,000, 1,500, 2,000, and 2,150 rpm under 36% relative humidity for each M:T condition of 1.2, 1.8, 2.4, and 3.0, respectively, a procedure described in detail elsewhere.[89,93,127] Immediately after spin coating, each sample was removed from the humidity-controlled chamber and placed on a 110 °C hot plate with a minimum period of 12 hrs to crosslink the oxide, termed as "aging." Aging conditions were optimized to prevent initial dewetting and to assure sufficient oxide connectivity to survive calcination. After each spin coating of a film, the spin coating chamber (generic "Tupperware") was replaced to avoid effects of residual solvent vapor, as observed previously.[89] Glass, silicon, and fluorine-doped tin (FTO) substrates were used for SAXS, SEM, and electrochemistry, respectively. After aging, the films were calcined, 5 °C min^{-1} to 200 °C followed by 10 °C min^{-1} to variable temperatures ranging from 300 °C to 550 °C for a 12 hr soak whereas the 600 °C samples had a 1 hr soak.

Electrode preparation

FTO substrates (TEC-15, Hartford Glass, CT) were rinsed and scrubbed with DI water using Kimwipes until scrubbing produces an audible squeaking noise followed by rinsing and scrubbing with IPA wetted Kimwipes again in the same manner. The substrates were then sonicated in a soapy water bath (2 g L^{-1} deconex) for 30 min. The water and alcohol scrub and rinse steps were repeated as before. The resulting substrates were stored submerged in IPA until near the time of spin coating. Just prior to coating, the FTO substrates were removed from IPA, blown dry. The FTO substrates were held at 110 °C until the moment they were used for spin coating. An uncoated area for electrical contact was maintained by masking part of the substrate with high-temperature Kapton tape. After spin coating and aging as described above, the edges of the FTO substrates were cleaved to remove edge effects[89] where residual template solution can collect at the substrate edges, resulting in a locally varied film thickness. The uncoated side of each film was engraved with identifying marks for M:T, recipe number, and film number. The Kapton mask was then removed. The ≈ 1 mm portion of the film proximal to the Kapton mask exhibited an edge effect with local variation of film thickness and was removed by scraping away oxide film with glass prior to calcination. The final active area of each sample was determined by photography over a ruled grid and was analyzed using ImageJ.

X-ray scattering experiments

X-ray experiments were conducted using the SAXSLab Ganesha at the South Carolina SAXS collaborative (SCSC). A Xenocs GeniX 3D microfocus source was used with a copper target to produce monochromatic beam with a 0.154 nm wavelength. The instrument was calibrated prior to measurements using National Institute of Standards and Technology (NIST) reference material, 640d silicon powder with peak position at $2\theta = 28.44°$. A Pilatus 300k detector (Dectris) was used to collect the 2D scattering patterns with nominal pixel dimensions of 172×172 µm. SAXS data were acquired with an X-ray flux of ≈ 1.41 M photon per second upon the sample and a detector-to-sample distance of 1400 mm. Transmission SAXS data were measured to observe the purely in-plane morphology. The 2D images were azimuthally integrated to yield the scattering vector and intensity. GI-WAXS measurements were conducted with an incident angle (α_i) of 8° relative to the incident

Batteries & Supercaps

Research Article
doi.org/10.1002/batt.202200056

Chemistry Europe
European Chemical
Societies Publishing

beam. The GI-WAXS sample-to-detector distance was 112.1 mm with an X-ray flux of ≈ 39.2 M photon per second upon the sample. A Gaussian point-spread function was utilized to interpret scattering data as a result of grain-size broadening per the Scherrer formula.[128,129]

X-ray adsorption spectroscopy experiments

The M:T series at 520, 535, and 600 °C were measured at beamline 20-ID at the Advanced Photon Source (APS) using a Si (111) monochromator. The beam was focused using a Rh coated toroidal mirror at 2.5 mrad. The incident and transmitted X-Rays were monitored with ion chambers filled with 80% He and 20% N_2 gas. The samples were mounted at about 15° incident angle and the Nb fluorescence detected with a 4-element silicon drift detector. Since the substrate glass had a strong Zn fluorescence signal, the signal was attenuated with 300 μm of Al foil in front of the detector. Multiple scans (5–6) were summed to achieve good signal-to-noise which also verified that sample damage from the beam was negligible as no change was observed. MT1.8 films at 300, 350, and 450 °C in addition to the solid-state T-Nb_2O_5 and TT-Nb_2O_5 standards (*vide infra*) were measured at APS beamline 20-BM using a Si (111) monochromator and similar Rh coated toroidal mirror focusing arrangement. Here, the fluorescence was measured using a 13 element Ge detector with 10–12 scans for good signal-to-noise. The solid-state samples were finely ground powders mounted on Scotch® Magic™ tape (3 M), with 16 layers giving a good signal in transmission. The data were analyzed using the Demeter software package.[130] Considering a smooth transition between the endpoints of MT1.8–300 °C and MT2.4–600 °C samples with the latter selected for its strong Nb—O signal in the Fourier transform ($|\chi(R)|$). Intermediate sample data ($\chi(k)$) were fitted as a linear combination of the two endpoints.

Electron paramagnetic resonance

EPR samples were prepared using PMT stock described previously. Once an M:T = 3.0 template solution was prepared, aliquots were cast into 20 mL scintillation vials and allowed to evaporate to dryness at room temperature under 25 L min^{-1} of flowing dry air inside a generic Tupperware container. Once dry, samples were aged at 110 °C for a minimum of 24 hrs before calcined with conditions described previously. EPR data were collected on a Bruker EMX spectrometer operating at X-band. The resonant frequency was 9.78 GHz with a modulation amplitude of 5.0 G and a microwave power of 2.0 mW. Data represent an average of 16 measurements. Results are baseline corrected using measurements made in an empty resonator.

Scanning electron microscopy

Top-view images of calcined films were acquired with a Zeiss Gemini500 field emission SEM using an accelerating voltage of 5 keV and an in-lens secondary electron detector. The working distance was maintained at ≈ 4.5 mm and images were acquired at constant magnification of 500k. At least 85 measurements were made upon each feature (pore and walls) to derive statistical metrics. The wall thickness was measured as the diameter on an inscribed circle between neighboring pores as described elsewhere,[91] in addition pore diameter was measured using an inscribed circle. Pore size and wall-thickness data are presented as mean values with the standard-error-of-the-mean. Cross-sectional SEM was used to determine film thickness.

Inductively coupled plasma mass spectrometry

A series of films prepared on FTO substrates were cut to ≈ 1 cm^2 of the niobia coating. ImageJ analysis was used to account for the specific substrate area as previously described. These films along with FTO blanks were heated in a Teflon vessel containing 70% HNO_3 (trace metal grade), 37% HCl (trace metal grade), and 48% HF (trace metal grade) (1:3:0.5 mL) respectively at 180 °C for 12 h before solutions were diluted with water (18.2 MΩ cm) to 50 mL volume and measured using a Thermo-Finnigan Element XR inductively coupled plasma mass spectrometry (ICP-MS). The instrument was calibrated using a range of concentrations spanning those of the measured samples. A range of digestion solutions were screened in a previous work, demonstrating the above solution is sufficient for complete digestion of niobia. These data were used to calculate the niobia mass per unit area for each sample condition.[21]

Electrochemical analysis

Electrochemical measurements were conducted using a three-electrode setup with a BioLogic SP-150 potentiostat. All measurements were performed in an argon-filled glovebox (<1 ppm O_2, <1 ppm H_2O). The working electrodes were porous niobia prepared using PMT on FTO substrates as described above. The working electrode was held by a home-built titanium metal clamp to assure ohmic contact to the FTO. All potentials are reported versus a Li/Li$^+$ reference electrode. The counter electrode was also lithium foil ≈ 540 mm^2 in surface area. All lithium foils were scraped until shiny just prior to immersion in electrolyte. The electrolyte solution was 1.0 M LiClO$_4$ in propylene carbonate. A series of diagnostic cyclic voltammograms and electrochemical impedance spectroscopy measurements were used to verify ohmic contact. The working electrode was then held at 1.2 V for 20 min before cycling from 1.2 to 3.0 V repeatedly 20 times at 10 mV s^{-1} to remove trace contaminants. A series of 21 logarithmically spaced sweeps ranging in rate from 1000 to 3.2 mV s^{-1} were run in sequence starting from 1.2 V versus Li/Li$^+$. There was a 3 min hold period at the end of each sweep to allow the electrode to equilibrate. Mass normalization was based upon the film area and ICP-MS measurements with identical samples.

Electrochemical data was imported into MATLAB 2018b using custom scripts and functions. The b-value metrics were determined as a difference between anodic peak currents and their corresponding voltage sweep rates; the corresponding voltage sweep rate for each b-value was the moving mean between the used voltage sweep rates. The determination of surface-limited threshold (SLT) was interpolated between b-value points as a function of corresponding voltage sweep rate. The standard error of this interpolation was estimated using Rolle's theorem. Parallel and series model fitting was done using the MATLAB non-linear regression function with the corresponding equations for each model. Non-linear fitting used mass-normalized current data, initial values close to expected values, a Cauchy weighting function for robust fitting, and a maximum number of iterations of 250,000. Fitting values generated from the non-linear regression function were passed through a gradient function to determine the corresponding predicted b-value of each model.

Solid-state synthesis of Nb_2O_5

Synthesis was adapted from elsewhere.[24] In brief, NbO_2 powder were calcined in alumina crucibles for 24 hrs with a 10 °C min^{-1} ramp rate at 350 and 600 °C to yield TT-Nb_2O_5 and T-Nb_2O_5

polymorphs respectively before allowed to cool to room temperature.

DFT calculations

Spin polarized DFT calculations were performed using the VASP[131] with projector augmented wave (PAW) pseudo potentials.[132] The generalized gradient approximation of Perdew-Burke-Ernzerhof (GGA-PBE) was used for the exchange-correlation functional.[133] The calculated lattice parameters for orthorhombic Nb_2O_5 are $a = 6.333$ Å, $b = 29.584$ Å, and $c = 3.813$ Å, which agree well with previously calculated values.[26] The O-rich (001) surface was modeled using a periodic slab containing five unit cells along the c-direction with one unit each along the a- and b-direction as shown in Figure S4(a). A vacuum gap of 15 Å was used along the surface normal direction (c-direction) to separate the slab from its periodic image. During geometry optimization, the atoms in the middle layer were fixed at their relaxed bulk positions to maintain the bulk phase, whereas all other atoms were allowed to fully relax until the residual forces become smaller than 0.02 eVÅ^{-1}. A plane-wave energy cutoff of 500 eV was used and the Brillouin zone of the (001) surface model was sampled using a $(4 \times 2 \times 1)$ Monkhorst-Pack[134] k-point mesh.

Acknowledgements

Conflict of Interest

The authors declare no conflict of interest.

Data Availability Statement

The data that support the findings of this study are available from the corresponding author upon reasonable request.

[1] J. W. Long, B. Dunn, D. R. Rolison, H. S. White, *Adv. Energy Mater.* **2020**, *10*, 2002457.
[2] P. F. Smith, K. J. Takeuchi, A. C. Marschilok, E. S. Takeuchi, *Acc. Chem. Res.* **2017**, *50*, 544.
[3] P. Albertus, V. Anandan, C. Ban, N. Balsara, I. Belharouak, J. Buettner-Garrett, Z. Chen, C. Daniel, M. Doeff, N. J. Dudney, B. Dunn, S. J. Harris, S. Herle, E. Herbert, S. Kalnaus, J. A. Libera, D. Lu, S. Martin, B. D. McCloskey, M. T. McDowell, Y. S. Meng, J. Nanda, J. Sakamoto, E. C. Self, S. Tepavcevic, E. Wachsman, C. Wang, A. S. Westover, J. Xiao, T. Yersak, *ACS Energy Lett.* **2021**, *6*, 1399.
[4] S. Fleischmann, J. B. Mitchell, R. Wang, C. Zhan, D. Jiang, V. Presser, V. Augustyn, *Chem. Rev.* **2020**, *120*, 6738.
[5] J. Maier, *Faraday Discuss.* **2015**, *176*, 17.
[6] J. M. Szeifert, J. M. Feckl, D. Fattakhova-Rohlfing, Y. Liu, V. Kalousek, J. Rathousky, T. Bein, *J. Am. Chem. Soc.* **2010**, *132*, 12605.
[7] J. B. Goodenough, Y. Kim, *Chem. Mater.* **2010**, *22*, 587.
[8] J.-M. Tarascon, M. Armand, In *Materials for Sustainable Energy*, Co-Published with Macmillan Publishers Ltd, UK, **2010**, pp. 171–179.
[9] H. Li, A. Liu, N. Zhang, Y. Wang, S. Yin, H. Wu, J. R. Dahn, *Chem. Mater.* **2019**, *31*, 7574.
[10] C. Costentin, T. R. Porter, J.-M. Savéant, *ACS Appl. Mater. Interfaces* **2017**, *9*, 8649.
[11] T. Brousse, D. Bélanger, J. W. Long, *J. Electrochem. Soc.* **2015**, *162*, A5185.
[12] V. Augustyn, P. Simon, B. Dunn, *Energy Environ. Sci.* **2014**, *7*, 1597.
[13] B. E. Conway, V. Birss, J. Wojtowicz, *J. Power Sources* **1997**, *66*, 1.
[14] B. E. Conway, *J. Electrochem. Soc.* **1991**, *138*, 1539.
[15] C. Choi, D. S. Ashby, D. M. Butts, R. H. DeBlock, Q. Wei, J. Lau, B. Dunn, *Nat. Rev. Mater.* **2020**, *5*, 5.
[16] S. Trasatti, G. Buzzanca, *J. Electroanal. Chem. Interfacial Electrochem.* **1971**, *29*, A1.
[17] J. P. Zheng, T. R. Jow, *J. Electrochem. Soc.* **1995**, *142*, L6.
[18] J. P. Zheng, P. J. Cygan, T. R. Jow, *J. Electrochem. Soc.* **1995**, *142*, 2699.
[19] K. Brezesinski, J. Wang, J. Haetge, C. Reitz, S. O. Steinmueller, S. H. Tolbert, B. M. Smarsly, B. Dunn, T. Brezesinski, *J. Am. Chem. Soc.* **2010**, *132*, 6982.
[20] V. Augustyn, J. Come, M. A. Lowe, J. W. Kim, P.-L. Taberna, S. H. Tolbert, H. D. Abruña, P. Simon, B. Dunn, *Nat. Mater.* **2013**, *12*, 518.
[21] W. van den Bergh, H. N. Lokupitiya, N. A. Vest, B. Reid, S. Guldin, M. Stefik, *Adv. Funct. Mater.* **2021**, *31*, 2007826.
[22] J. W. Kim, V. Augustyn, B. Dunn, *Adv. Energy Mater.* **2012**, *2*, 141.
[23] A. A. Lubimtsev, P. R. C. Kent, B. G. Sumpter, P. Ganesh, *J. Mater. Chem. A* **2013**, *1*, 14951.
[24] K. J. Griffith, A. C. Forse, J. M. Griffin, C. P. Grey, *J. Am. Chem. Soc.* **2016**, *138*, 8888.
[25] S. Li, Q. Xu, E. Uchaker, X. Cao, G. Cao, *CrystEngComm* **2016**, *18*, 2532.
[26] D. Chen, J.-H. Wang, T.-F. Chou, B. Zhao, M. A. El-Sayed, M. Liu, *J. Am. Chem. Soc.* **2017**, *139*, 7071.
[27] Q. Deng, Y. Fu, C. Zhu, Y. Yu, *Small* **2019**, *15*, 1804884.
[28] C. Li, Q. Li, Y. V. Kaneti, D. Hou, Y. Yamauchi, Y. Mai, *Chem. Soc. Rev.* **2020**, *49*, 4681.
[29] X. Xu, B. Tian, S. Zhang, J. Kong, D. Zhao, B. Liu, *Anal. Chim. Acta* **2004**, *519*, 31.
[30] W. Luo, Y. Li, J. Dong, J. Wei, J. Xu, Y. Deng, D. Zhao, *Angew. Chem.* **2013**, *125*, 10699.
[31] L. Kong, C. Zhang, S. Zhang, J. Wang, R. Cai, C. Lv, W. Qiao, L. Ling, D. Long, *J. Mater. Chem. A* **2014**, *2*, 17962.
[32] E. Lim, H. Kim, C. Jo, J. Chun, K. Ku, S. Kim, H. I. Lee, I.-S. Nam, S. Yoon, K. Kang, J. Lee, *ACS Nano* **2014**, *8*, 8968.
[33] E. Lim, C. Jo, H. Kim, M.-H. Kim, Y. Mun, J. Chun, Y. Ye, J. Hwang, K.-S. Ha, K. C. Roh, K. Kang, S. Yoon, J. Lee, *ACS Nano* **2015**, *9*, 7497.
[34] F. Idrees, J. Hou, C. Cao, F. K. Butt, I. Shakir, M. Tahir, F. Idrees, *Electrochim. Acta* **2016**, *216*, 332.
[35] G. Ma, K. Li, Y. Li, B. Gao, T. Ding, Q. Zhong, J. Su, L. Gong, J. Chen, L. Yuan, B. Hu, J. Zhou, K. Huo, *ChemElectroChem* **2016**, *3*, 1360.
[36] H. Song, J. Fu, K. Ding, C. Huang, K. Wu, X. Zhang, B. Gao, K. Huo, X. Peng, P. K. Chu, *J. Power Sources* **2016**, *328*, 599.
[37] J. Y. Cheong, J.-W. Jung, D.-Y. Youn, C. Kim, S. Yu, S.-H. Cho, K. R. Yoon, I.-D. Kim, *J. Power Sources* **2017**, *360*, 434.

Batteries & Supercaps

Research Article
doi.org/10.1002/batt.202200056

Chemistry Europe
European Chemical
Societies Publishing

[38] S. Lou, X. Cheng, L. Wang, J. Gao, Q. Li, Y. Ma, Y. Gao, P. Zuo, C. Du, G. Yin, *J. Power Sources* **2017**, *361*, 80.

[39] G. Luo, H. Li, D. Zhang, L. Gao, T. Lin, *Electrochim. Acta* **2017**, *235*, 175.

[40] C. Shi, K. Xiang, Y. Zhu, W. Zhou, X. Chen, H. Chen, *Ceram. Int.* **2017**, *43*, 12388.

[41] M. Y. Song, N. R. Kim, H. J. Yoon, S. Y. Cho, H.-J. Jin, Y. S. Yun, *ACS Appl. Mater. Interfaces* **2017**, *9*, 2267.

[42] H. Sun, L. Mei, J. Liang, Z. Zhao, C. Lee, H. Fei, M. Ding, J. Lau, M. Li, C. Wang, X. Xu, G. Hao, B. Papandrea, I. Shakir, B. Dunn, Y. Huang, X. Duan, *Science* **2017**, *356*, 599.

[43] H. Yang, H. Xu, L. Wang, L. Zhang, Y. Huang, X. Hu, *Chem. Eur. J.* **2017**, *23*, 4203.

[44] J. Zhai, Y. Wu, X. Zhao, Q. Yang, *J. Alloys Compd.* **2017**, *715*, 275.

[45] Z. Chen, H. Li, X. Lu, L. Wu, J. Jiang, S. Jiang, J. Wang, H. Dou, X. Zhang, *ChemElectroChem* **2018**, *5*, 1516.

[46] B. Deng, T. Lei, W. Zhu, L. Xiao, J. Liu, *Adv. Funct. Mater.* **2018**, *28*, 1704330.

[47] Y. Jiao, H. Zhang, H. Zhang, A. Liu, Y. Liu, S. Zhang, *Nano Res.* **2018**, *11*, 4673.

[48] L. Kong, X. Liu, J. Wei, S. Wang, B. B. Xu, D. Long, F. Chen, *Nanoscale* **2018**, *10*, 14165.

[49] J. Liao, R. Tan, Z. Kuang, C. Cui, Z. Wei, X. Deng, Z. Yan, Y. Feng, F. Li, C. Wang, J. Ma, *Chin. Chem. Lett.* **2018**, *29*, 1785.

[50] S. Zhang, J. Wu, J. Wang, W. Qiao, D. Long, L. Ling, *J. Power Sources* **2018**, *396*, 88.

[51] S. Hemmati, G. Li, X. Wang, Y. Ding, Y. Pei, A. Yu, Z. Chen, *Nano Energy* **2019**, *56*, 118.

[52] S. Jiang, S. Dong, L. Wu, Z. Chen, L. Shen, X. Zhang, *J. Electroanal. Chem.* **2019**, *842*, 82.

[53] J. W. Kim, S.-O. Kim, H.-S. Kim, *Int. J. Energy Res.* **2019**, *43*, 4359.

[54] D. Li, J. Shi, H. Liu, C. Liu, G. Dong, H. Zhang, Y. Yang, G. Lu, H. Wang, *Sustain. Energy Fuels* **2019**, *3*, 1055.

[55] J. Hu, J. Li, K. Wang, H. Xia, *Electrochim. Acta* **2020**, *331*, 135364.

[56] W. Hu, S. Zhang, W. Zhang, M. Wang, F. Feng, *J. Nanopart. Res.* **2020**, *22*, 57.

[57] Z. Hu, Q. He, Z. Liu, X. Liu, M. Qin, B. Wen, W. Shi, Y. Zhao, Q. Li, L. Mai, *Sci. J.* **2020**, *65*, 1154.

[58] J. Kang, H. Zhang, Z. Zhan, Y. Li, M. Ling, X. Gao, *ACS Appl. Energ. Mater.* **2020**, *3*, 11841.

[59] S. Kim, J. Hwang, J. Lee, J. Lee, *Sci. Adv.* **2020**, *6*, eabb3814.

[60] Y. Li, Y. Wang, G. Cui, T. Zhu, J. Zhang, C. Yu, J. Cui, J. Wu, H. H. Tan, Y. Zhang, Y. Wu, *ACS Appl. Energ. Mater.* **2020**, *3*, 12037.

[61] Y. Li, R. Wang, W. Zheng, Q. Zhao, S. Sun, G. Ji, S. Li, X. Fan, C. Xu, *Mater. Technol.* **2020**, *35*, 625.

[62] Y. Lian, D. Wang, S. Hou, C. Ban, J. Zhao, H. Zhang, *Electrochim. Acta* **2020**, *330*, 135204.

[63] D. Liang, L. Hu, L. Wang, L. Liu, S. Liang, L. Yang, N. Zhou, C. Liang, *ChemNanoMat* **2020**, *6*, 73.

[64] Z. Liu, W. Dong, J. Wang, C. Dong, Y. Lin, I.-W. Chen, F. Huang, *iScience* **2020**, *23*, 100767.

[65] P. Nagaraju, R. Vasudevan, A. Alsalme, A. Alghamdi, M. Arivanandhan, R. Jayavel, *Nanomaterials* **2020**, *10*, 160.

[66] X. Qu, Y. Liu, B. Li, B. Xing, G. Huang, C. Zhang, S. W. Hong, J. Yu, Y. Cao, *Energy Fuels* **2020**, *34*, 3887.

[67] L. She, F. Zhang, C. Jia, L. Kang, Q. Li, X. He, J. Sun, Z. Lei, Z.-H. Liu, *J. Colloid Interface Sci.* **2020**, *573*, 1.

[68] X. Zhai, J. Liu, Y. Zhao, C. Chen, X. Zhao, J. Li, H. Jin, *Appl. Surf. Sci.* **2020**, *499*, 143905.

[69] H. Ding, Z. Song, K. Feng, H. Zhang, H. Zhang, X. Li, *J. Solid State Chem.* **2021**, *299*, 122136.

[70] J. Jin, J. Cai, X. Wang, Z. Sun, Y. Song, J. Sun, *FlatChem* **2021**, *27*, 100236.

[71] S. Ouendi, C. Arico, F. Blanchard, J.-L. Codron, X. Wallart, P. L. Taberna, P. Roussel, L. Clavier, P. Simon, C. Lethien, *Energy Storage Mater.* **2019**, *16*, 581.

[72] R. Kang, S. Li, B. Zou, X. Liu, Y. Zhao, J. Qiu, G. Li, F. Qiao, J. Lian, *J. Alloys Compd.* **2021**, *865*, 158824.

[73] E. Lim, C. Jo, M. S. Kim, M.-H. Kim, J. Chun, H. Kim, J. Park, K. C. Roh, K. Kang, S. Yoon, J. Lee, *Adv. Funct. Mater.* **2016**, *26*, 3711.

[74] R. Bi, N. Xu, H. Ren, N. Yang, Y. Sun, A. Cao, R. Yu, D. Wang, *Angew. Chem.* **2020**, *132*, 4895.

[75] B.-A. Mei, J. Lau, T. Lin, S. H. Tolbert, B. S. Dunn, L. Pilon, *J. Phys. Chem. C* **2018**, *122*, 24499.

[76] J. S. Ko, C.-H. Lai, J. W. Long, D. R. Rolison, B. Dunn, J. Nelson Weker, *ACS Appl. Mater. Interfaces* **2020**, *12*, 14071.

[77] N. Li, X. Lan, L. Wang, Y. Jiang, S. Guo, Y. Li, X. Hu, *ACS Appl. Mater. Interfaces* **2021**, *13*, 16445.

[78] X. Ge, C. Gu, Z. Yao, J. Sun, X. Wang, J. Tu, *Chem. Eng. J.* **2018**, *338*, 211.

[79] Z. Song, H. Li, W. Liu, H. Zhang, J. Yan, Y. Tang, J. Huang, H. Zhang, X. Li, *Adv. Mater.* **2020**, *32*, 2001001.

[80] W. V. Metanomski, Ed., *Compendium of Macromolecular Nomenclature*, 1st ed., International Union of Pure and Applied Chemistry., **1991**.

[81] J.-Y. Shin, J. H. Joo, D. Samuelis, J. Maier, *Chem. Mater.* **2012**, *24*, 543.

[82] H.-S. Kim, J. B. Cook, H. Lin, J. S. Ko, S. H. Tolbert, V. Ozolins, B. Dunn, *Nat. Mater.* **2017**, *16*, 454.

[83] S. Zhang, G. Liu, W. Qiao, J. Wang, L. Ling, *J. Colloid Interface Sci.* **2020**, *562*, 193.

[84] J. Ye, P. Shea, A. C. Baumgaertel, S. A. Bonev, M. M. Biener, M. Bagge-Hansen, Y. M. Wang, J. Biener, B. C. Wood, *Chem. Mater.* **2018**, *30*, 8871.

[85] G. Wang, Y. Ling, Y. Li, *Nanoscale* **2012**, *4*, 6682.

[86] J. A. Yuwono, P. Burr, C. Galvin, A. Lennon, *ACS Appl. Mater. Interfaces* **2021**, *13*, 1791.

[87] A. L. Viet, M. V. Reddy, R. Jose, B. V. R. Chowdari, S. Ramakrishna, *J. Phys. Chem. C* **2010**, *114*, 664.

[88] J. Meng, Q. He, L. Xu, X. Zhang, F. Liu, X. Wang, Q. Li, X. Xu, G. Zhang, C. Niu, Z. Xiao, Z. Liu, Z. Zhu, Y. Zhao, L. Mai, *Adv. Energy Mater.* **2019**, *9*, 1802695.

[89] A. Sarkar, M. Stefik, *J. Mater. Chem. A* **2017**, *5*, 11840.

[90] H. N. Lokupitiya, A. Jones, B. Reid, S. Guldin, M. Stefik, *Chem. Mater.* **2016**, *28*, 1653.

[91] K. A. Lantz, N. B. Clamp, W. van den Bergh, A. Sarkar, M. Stefik, *Small* **2019**, *15*, 1900393.

[92] A. Sarkar, A. Thyagarajan, A. Cole, M. Stefik, *Soft Matter* **2019**, *15*, 5193.

[93] A. Sarkar, L. Evans, M. Stefik, *Langmuir* **2018**, *34*, 5738.

[94] A. Vu, Y. Qian, A. Stein, *Adv. Energy Mater.* **2012**, *2*, 1056.

[95] M. Stefik, *J. Mater. Res.* **2021**.

[96] M. C. Orilall, U. Wiesner, *Chem. Soc. Rev.* **2011**, *40*, 520.

[97] C. Robertus, W. H. Philipse, J. G. H. Joosten, Y. K. Levine, *J. Chem. Phys.* **1989**, *90*, 4482.

[98] M. A. Sahiner, A. Nabizadeh, D. Rivella, L. Cerqueira, J. Hachlica, R. Morea, J. Gonzalo, J. C. Woicik, *J. Phys. Conf. Ser.* **2016**, *712*, 012103.

[99] M. T. Vandenborre, B. Poumellec, J. Livage, *J. Solid State Chem.* **1989**, *83*, 105.

[100] M. T. Vandenborre, B. Poumellec, C. Alquier, J. Livage, *J. Non-Cryst. Solids* **1989**, *108*, 333.

[101] I. Andoni, J. M. Ziegler, G. Jha, C. A. Gadre, H. Flores-Zuleta, S. Dai, S. Qiao, M. Xu, V. T. Chen, X. Pan, R. M. Penner, *ACS Appl. Energ. Mater.* **2021**, acsaem.1c00580.

[102] N. Özer, T. Barreto, T. Büyüklimanli, C. M. Lampert, *Sol. Energy Mater. Sol. Cells* **1995**, *36*, 433.

[103] A. S. Foster, A. L. Shluger, R. M. Nieminen, *Phys. Rev. Lett.* **2002**, *89*, 225901.

[104] H.-W. Huang, Z.-G. Ye, M. Dong, W.-L. Zhu, X.-Q. Feng, *Jpn. J. Appl. Phys.* **2002**, *41*, L713.

[105] E. Talik, J. Kisielewski, P. Zajdel, A. Guzik, E. Wierzbicka, A. Kania, J. Kusz, S. Miga, M. Szubka, *Opt. Mater.* **2019**, *91*, 355.

[106] A. Sahai, N. Goswami, *Ceram. Int.* **2014**, *40*, 14569.

[107] J.-W. Sun, L.-S. Kang, J.-S. Kim, M.-R. Joung, S. Nahm, T.-G. Seong, C.-Y. Kang, J.-H. Kim, *Acta Mater.* **2011**, *59*, 5434.

[108] J. Cao, D. Zhang, Y. Yue, T. Pakornchote, T. Bovornratanaraks, M. Sawangphruk, X. Zhang, J. Qin, *Mater. Today* **2021**, *21*, 100824.

[109] S. Yang, Y. Liu, Y. Hao, X. Yang, W. A. Goddard III, X. L. Zhang, B. Cao, *Adv. Sci.* **2018**, *5*, 1700659.

[110] E. Knözinger, O. Diwald, M. Sterrer, *J. Mol. Catal. A* **2000**, *162*, 83.

[111] M. Sterrer, O. Diwald, E. Knözinger, *J. Phys. Chem. B* **2000**, *104*, 3601.

[112] J. M. Coronado, A. J. Maira, J. C. Conesa, K. L. Yeung, V. Augugliaro, J. Soria, *Langmuir* **2001**, *17*, 5368.

[113] M. R. Lukatskaya, B. Dunn, Y. Gogotsi, *Nat. Commun.* **2016**, *7*, 12647.

[114] H. Lindström, S. Södergren, A. Solbrand, H. Rensmo, J. Hjelm, A. Hagfeldt, S.-E. Lindquist, *J. Phys. Chem. B* **1997**, *101*, 7717.

[115] V. Murray, D. S. Hall, J. R. Dahn, *J. Electrochem. Soc.* **2019**, *166*, A329.

[116] T. Marks, S. Trussler, A. J. Smith, D. Xiong, J. R. Dahn, *J. Electrochem. Soc.* **2011**, *158*, A51.

[117] N. Kumagai, K. Tanno, T. Nakajima, N. Watanabe, *Electrochim. Acta* **1983**, *28*, 17.

[118] T.-C. Liu, W. G. Pell, B. E. Conway, S. L. Roberson, *J. Electrochem. Soc.* **1998**, *145*, 1882.

[119] H. Kim, E. Lim, C. Jo, G. Yoon, J. Hwang, S. Jeong, J. Lee, K. Kang, *Nano Energy* **2015**, *16*, 62.

[120] D. Chao, R. DeBlock, C.-H. Lai, Q. Wei, B. Dunn, H. J. Fan, *Adv. Mater.* **2021**, *33*, 2103736.

[121] S. Moitzheim, S. D. Gendt, P. M. Vereecken, *J. Electrochem. Soc.* **2019**, *166*, A1.

[122] V. Daramalla, G. Venkatesh, B. Kishore, N. Munichandraiah, S. B. Krupanidhi, *J. Electrochem. Soc.* **2018**, *165*, A764.

[123] J. Han, A. Hirata, J. Du, Y. Ito, T. Fujita, S. Kohara, T. Ina, M. Chen, *Nano Energy* **2018**, *49*, 354.

[124] W. S. Shih, S. J. Young, L. W. Ji, W. Water, H. W. Shiu, *J. Electrochem. Soc.* **2011**, *158*, H609.

[125] D. B. G. Williams, M. Lawton, *J. Org. Chem.* **2010**, *75*, 8351.

[126] L. J. Fetters, D. J. Lohse, D. Richter, T. A. Witten, A. Zirkel, *Macromolecules* **1994**, *27*, 4639.

[127] H. N. Lokupitiya, M. Stefik, *Nanoscale* **2017**, *9*, 1393.

[128] A. L. Patterson, *Phys. Rev.* **1939**, *56*, 978.

[129] P. Scherrer, *Math. Phys.* **1918**, *2*, 98.

[130] B. Ravel, M. Newville, *J. Synchrotron Radiat.* **2005**, *12*, 537.

[131] G. Kresse, J. Furthmüller, *Comput. Mater. Sci.* **1996**, *6*, 15.

[132] P. E. Blöchl, *Phys. Rev. B* **1994**, *50*, 17953.

[133] J. P. Perdew, K. Burke, M. Ernzerhof, *Phys. Rev. Lett.* **1996**, *77*, 3865.

[134] H. J. Monkhorst, J. D. Pack, *Phys. Rev. B* **1976**, *13*, 5188.

[135] F. Crameri, G. E. Shephard, P. J. Heron, *Nat. Commun.* **2020**, *11*, 5444.

[136] F. Crameri, *Geos* **2018**, *11*, 2541.